

ALMA FACTS III. High-Resolution CO(2-1)/CO(1-0) Maps of Twelve Nearby Galaxies

AMANDA M LEE,¹ JIN KODA,¹ FUMI EGUSA,² AKIHIKO HIROTA,^{3,4} SHINYA KOMUGI,^{1,5,6} FUMIYA MAEDA,⁷ AND TSUYOSHI SAWADA^{3,4}

¹*Stony Brook University, Stony Brook, NY 11743-3800, USA*

²*Institute of Astronomy, Graduate School of Science, The University of Tokyo, 2-21-1 Osawa, Mitaka, Tokyo 181-0015, Japan*

³*National Astronomical Observatory of Japan, Los Abedules 3085 Office 701, Vitacura, Santiago 763 0414, Chile*

⁴*Joint ALMA Observatory, Alonso de Córdova 3107, Vitacura, Santiago 763 0355, Chile*

⁵*Division of Liberal Arts, Kogakuin University, 2665-1 Nakano-cho, Hachioji, Tokyo 192-0015, Japan*

⁶*National Astronomical Observatory of Japan, 2-21-1 Osawa, Mitaka, Tokyo 181-8588, Japan*

⁷*Research Center for Physics and Mathematics, Osaka Electro-Communication University, 18-8 Hatsucho, Neyagawa, Osaka, 572-8530, Japan*

ABSTRACT

We present early results from a high-resolution analysis (~ 100 - 200 pc) of the CO(2-1)/CO(1-0) line ratio in twelve nearby galaxies. We use new ALMA CO(1-0) observations from the Fundamental CO(1-0) Transition Survey (FACTS), and re-imaged CO(2-1) data from PHANGS. We make empirical classifications based on the optical and molecular gas morphologies, which show clear systematic trends in the variation of R_{21} as a function of galactic structure. The sample includes barred and unbarred, and flocculent galaxies. The barred spiral galaxies follow a general trend: R_{21} is high in the center, low along the bar, increases at the bar ends, and then declines in the outer parts of the disk. The structure dependence suggests the importance of galactic dynamics on molecular gas evolution, and consequently on star formation, in galaxies. R_{21} fluctuates in the spiral arms for both barred and unbarred galaxies. HII regions increase R_{21} locally in their surrounding gas and are often associated with galactic structures. Together, R_{21} varies systematically as a function of galactic structure, dynamics, and star formation activity.

1. INTRODUCTION

The two lowest transitions, $J=1-0$ and $2-1$, of ^{12}CO are often used to trace the bulk molecular gas in galaxies. Both emissions likely originate from the same region within the molecular gas even when it is not resolved (e.g., Sakamoto et al. 1994, 1997; Oka et al. 1998b). Therefore, their line ratio CO($J=2-1$)/CO($J=1-0$) ($\equiv R_{21}$) can trace and constrain the physical conditions of the molecular gas (Goldreich & Kwan 1974; Scoville & Solomon 1974; van der Tak et al. 2007). CO is excited by collisions with H_2 molecules, and its emissions travel through regions of high CO opacity. Hence, R_{21} is determined by the kinetic temperature T_k , H_2 volume density n_{H_2} , and the CO column density N_{CO} . It can increase due to gas compression before star formation or due to gas heating after star formation (Koda et al. 2012). The variations of R_{21} across galaxies can thus show the evolution of the bulk molecular gas in the galactic disks.

Studies in the Milky Way (MW) have shown systematic variations in R_{21} within and amongst molecular clouds, and in the Galactic disk (Hasegawa 1997,

for a review). These studies have classified molecular gas according to R_{21} as low-ratio gas (LRG) with $R_{21} < 0.7$, high-ratio gas (HRG) with $R_{21} > 0.7$, and very-high ratio gas (VHRG) $R_{21} > 1.0$. For example, R_{21} varies between and within star-forming and non-star-forming molecular clouds. Sakamoto et al. (1994) and more recently Nishimura et al. (2015) mapped the star-forming Orion molecular clouds, and found that R_{21} ranges from 0.5 to 1.0 between the main ridge and peripheries of Orion A. Falgarone et al. (1998) studied non-star-forming molecular clouds and found they have roughly uniform $R_{21} \sim 0.65$. In the Galactic disk, R_{21} radially decreases (Sakamoto et al. 1997), with azimuthal variations, i.e., LRG in the interarms and HRG in the spiral arms. In the Galactic center, the molecular gas exhibits distinctive properties than gas in the disk, and can be excited to high $R_{21} > 0.7$, and occasionally, very-high ratios $R_{21} > 1.0$ (Oka et al. 1996, 1998b; Sawada et al. 2001). Overall, the ratio varies from 0.96 in the central kiloparsec region of the MW, while the typical disk value is 0.6-0.7 (Sawada et al. 2001). VHRG with $R_{21} > 1.0$ is relatively rare and is typically found

in the close vicinity of star formation, e.g. due to interaction with supernovae, or in the galactic center (Oka et al. 1996; Seta et al. 1998).

There have been many efforts to characterize R_{21} in external galaxies. However, previous measurements were often hindered by challenges in calibration, especially since R_{21} intrinsically has a relatively small dynamic range (only a factor of ~ 2 -3 variation; Garcia-Burillo et al. 1993; Crosthwaite et al. 2002; Lundgren et al. 2004; Crosthwaite & Turner 2007; Koda et al. 2012; Yajima et al. 2021; Leroy et al. 2022). The calibration issue often led to high $R_{21} > 1$ over large regions of the galaxies, seemingly indicating widespread optically-thin CO gas, which is not very likely. Spatial variations in R_{21} in external galaxies began to become apparent with improvements in calibration and techniques (e.g., Koda et al. 2012). In particular, with the advent of ALMA, studies of R_{21} have become increasingly possible (Koda et al. 2020; Egusa et al. 2022; Maeda et al. 2022; den Brok et al. 2023).

High-resolution studies of R_{21} remain relatively scarce and are typically case-studies, or due to limited coverage, focus on particular regions in galaxies (Egusa et al. 2022; Maeda et al. 2022; den Brok et al. 2023; Koda et al. 2025). These studies have found R_{21} values similar to those of Galactic studies as well as indications of R_{21} trends with respect to galactic structures. Beyond case-studies, it is clear that a survey of R_{21} in nearby galaxies at high-resolution and with well-calibrated data, is needed to understand the general evolution of molecular gas and their physical conditions. While there are existing surveys of R_{21} variations (e.g., Yajima et al. 2021; Leroy et al. 2022), they are at lower sensitivity and resolution, and the compared CO(1-0) and CO(2-1) data were often observed from different telescopes. As a result, overall systematic trends were not clear.

In this paper, we analyze R_{21} in twelve nearby galaxies using new high-resolution CO(1-0) data from the ALMA-FACTS survey and reimaged CO(2-1) data from the PHANGS-ALMA survey (Leroy et al. 2021). We present early results, which already empirically show systematic trends as a function of galactic structure. This is the third paper of the ALMA-FACTS Survey. R_{21} on kpc-scales in the same twelve sample galaxies using the ALMA Total Power (TP) component has been studied (ALMA-FACTS Paper II; Komugi et al. 2025). We plan multi-wavelength comparisons for future studies.

2. OBSERVATIONS AND DATA REDUCTION

The FACTS sample of 12 galaxies (Table 1; Figure 1) is the complete set of all the galaxies com-

mon to the PHANGS-ALMA (Leroy et al. 2021), Spitzer-SINGS (Kennicutt et al. 2003), and Herschel-KINGFISH surveys (Kennicutt et al. 2011), except one galaxy (NGC 4569) whose redshifted frequency is near the edge of the ALMA coverage and is not optimal for ALMA sensitivity. It spans a wide range of spiral arm/bar strength and SF activity. The design of the survey is discussed in a separate summary paper from the FACTS survey (Koda et al. in prep).

This section discusses the data reduction, mainly on the CO(2-1) data (Section 2.1). The CO(1-0) data reduction is discussed in a separate paper (Koda et al. in prep.), but is practically the same with one note in Section 2.2. This method has been discussed in depth and used by Koda et al. (2023) and Koda et al. (2025).

We used a common channel width of 5 km s^{-1} in CO(1-0) and CO(2-1). After the imaging discussed below, we smoothed the CO(1-0) and CO(2-1) data to a common beam size of $2.5''$ for the line ratio analysis.

Figure 1 shows the sample in *Spitzer* $3.6 \mu\text{m}$ dust emission from S4G (Sheth et al. 2010; S4G Team 2020) and SINGS (for NGC 3621, Kennicutt et al. 2003; SINGS Team 2020) to demonstrate the field-of-view (FoV) of the observations. The FoVs of the 12m+07m CO(2-1) observations (yellow contours), and consequently the R_{21} maps (section 4.1), cover the *inner* disks of the galaxies.

2.1. CO(2-1)

The twelve galaxies in our sample were observed in CO(J=2-1) with the ALMA 12m, 07m, and TP arrays, as a part of the PHANGS survey (Leroy et al. 2021). We obtained the raw archival data from projects 2012.1.00650.S (NGC 0628), 2015.1.00925.S (NGC 1512), 2015.1.00956.S (NGC 3351, 3627, 4254, and 4321), 2017.1.00886.L (NGC 1097, 3521, 3621, 4536, 4579, and 4826), and 2018.1.01651.S (NGC 1512). The procedure used for the TP data reduction is described in Koda et al. (2020). Here, we explain the data reduction of the 12m and 07m data. The 12m and 07m data were calibrated with the Common Astronomy Software Application (CASA; CASA Team et al. 2022) and imaged with Multichannel Image Reconstruction, Image Analysis, and Display (MIRIAD; Sault et al. 1995, 1996).

2.1.1. Calibration

To calibrate the archival measurement sets (MSs), we ran the distributed pipeline scripts from the observatory, either generated for the PI, or a generic pipeline script. Different versions (v.4.7.2, v.5.1.2, and v.5.4.1) of the CASA pipeline were used across the galaxy sample. We used v.4.7.2 for projects 2012.1.00650.S and 2015.1.00925.S, v.4.7.2 and v.5.4.1 for 2015.1.00956.S,

v.5.1.2 and v.5.4.1 for 2017.1.00886.L, and v.5.4.1 for 2018.1.01651.S.

To assess the data after calibration, we checked the calibrated amplitudes and phases of the bandpass and gain calibrators (point sources). We considered the calibration successful if their amplitudes were flat and constant as functions of channel and time, and the phases as functions of channel and time were concentrated about 0 degrees. The consistency between the 12m and 07m calibrated data was checked by looking at the galaxy amplitude plotted against uv distance.

For NGC 3621, the same gain calibrator was used across all of the archival 12m data (execution blocks) and had a weak amplitude of ~ 60 mJy. This resulted in relatively large phase errors even after the calibration. In this case, we also made plots of the bandpass and gain calibrators in the complex plane and checked that their calibrated data points were localized.

The standard flux calibration in the CASA pipeline was used for most galaxies. However, NGC 0628 was observed relatively early in the ALMA observatory operation, and the pipeline calibration returned too low a flux. Therefore, we measured the fluxes of gain and bandpass calibrators with respect to Uranus or Neptune when they were observed in NGC 0628 measurement sets, and applied the measured fluxes to the rest of measurement sets when neither Uranus nor Neptune was included.

2.1.2. Imaging

The 12m and 07m array data for each galaxy were imaged together in MIRIAD, instead of CASA, because it takes into account spatial variations in the point spread function (PSF) (Koda et al. 2023). To prepare for imaging in MIRIAD, we used the CASA tasks *split* and *mstransform* to split the narrowband spectral window (SPW) containing the CO(2-1) emission out from each 12m and 07m MS, and then to regrid them to a common velocity grid with channel width 5 km/s. These were converted into MIRIAD format. We used the average system temperature T_{sys} and integration times t_{int} from each MS following Koda et al. (2023). The invert task in MIRIAD was then performed on these 12m and 07m visibilities to produce the CO(2-1) data cubes. We used `robust = +2` (corresponding to natural weighting), `cellsize = 0.25''`, and a velocity coverage and width of 5 km/s matching those of the CO(1-0) data cubes (Koda et al. in prep).

We used the `mosssdi2` task in MIRIAD for cleaning. To identify regions where we may expect significant CO(2-1) emission, we first created masks for each galaxy by using its corresponding CO(1-0) signal-to-noise (SN) data

cube (Koda et al. in prep). The mask includes connected regions with at least one pixel with $\text{SN} \geq 3.5\sigma$ and 32 pixels with $\text{SN} \geq 2.5\sigma$, and then is expanded to include pixels with $\text{SN} \geq 1.5\sigma$. Using these masks, the dirty CO(2-1) cubes were cleaned in two steps: [1] within the mask and then [2] without a mask but cleaning the residual from [1] to recover emission that was potentially missed in the first step. We set a gain parameter of 0.05, `options=positive` (for cleaning within the mask in [1]), and 10^7 clean components per channel. The residual emission within the mask after the two-step cleaning were about $\sim 0.1\sigma$.

The cleaned 12m+07m data cubes were combined with the TP data cubes using the `immerge` task in MIRIAD. We identified velocity channels that were covered by both 12m+07m and TP data cubes, regridded the TP data spatially to the same grid as the 12m+07m data cube, and then combined the TP data cube to the primary-beam corrected 12m+07m cleaned data cube.

The RMS noise per 5 km/s channel for the 12m+07m+TP data was measured with the dirty 12m+07m cube combined with TP data. The RMS is measured in emission-free channels. They are in Table 2.

2.2. CO(1-0)

The data reduction for CO(1-0) is discussed in a separate paper (Koda et al., in prep.), but is practically the same as the one discussed above. The only difference is the very first step of imaging, where we did not have a reference cube to make a mask. We went through the full imaging process without any mask and generated a 12m+07m+TP cube in CO(1-0). A mask is made with this cube for the second imaging as discussed above.

3. MAPS

Figure 1 shows the FoVs of the CO(2-1) data on the Spitzer $3.6\mu\text{m}$ images. The corresponding RMS per channel maps for CO(2-1) are shown in Figure 2. The CO(2-1) data were imaged out to when the sensitivity drops to $1/3 \sim 33\%$ of the peak sensitivity of each pointing (primary beam). However, we restrict the analysis to the area where the sensitivity drops to 40-50% of the peak sensitivity, which is indicated by the black contours in Figure 2 (yellow contours in Figure 1). For most of the sample, multiple separate observations in CO(2-1) were taken to cover the entire field. Consequently, there are variations in the CO(2-1) sensitivity across the map for each galaxy, but for eleven out of the twelve galaxies, the sensitivities are roughly uniform within $\sim 20 - 30\%$ across the entire field, and drop towards the edge. NGC 4321 is an exception with the

northern part of the map having about twice lower sensitivity (i.e., twice higher noise) relative to the southern part. NGC 4321 had only two 12m MSs, one for the northern part and the other covering the southern part. Overall, to avoid the low sensitivity edges in the R_{21} analysis, we only include the region where the sensitivity drops to $1/2 \sim 50\%$ of the peak sensitivity for eleven of the galaxies, and to $\sim 40\%$ of the peak sensitivity for NGC 4321.

Figures 3 and 4 show the integrated intensity maps, $I_{\text{CO}(1-0)}$ and $I_{\text{CO}(2-1)}$, in CO(1-0) and CO(2-1) for all the 12 galaxies. The coverage of the CO(1-0) observations are slightly larger than the CO(2-1) observations. Unlike CO(2-1), the CO(1-0) observations cover the entire field in each execution, and thus have more or less uniform sensitivity across the field. Hence, the resulting coverage and variations in sensitivity across the R_{21} maps for each galaxy are mainly determined by the CO(2-1) observations.

To make the integrated intensity maps for each galaxy, we smoothed the CO(1-0) and CO(2-1) cubes to a common angular resolution of $2.5''$. We then regridded the CO(2-1) data spatially to the CO(1-0) data and applied a mask to the data cubes. The mask was based on the (cleaned) CO(1-0) signal-to-noise (SN) cube starting from volumes that have at least 80 pixels with $> 5.0\sigma$. This mask was then expanded spatially by $2.5''$ ($=10$ pixels in length) to include potential diffuse extended emission (if it exists). After applying this mask, the cubes were integrated along the velocity axis to produce the integrated intensity maps, and corresponding error maps were generated. The error in each pixel is calculated as $\text{RMS} \cdot \Delta v \cdot \sqrt{N}$, where RMS is the RMS noise per channel width Δv , and N is the number of channels included in the velocity integration.

These are shown in Figures 3 and 4. The colorbar scales for $I_{\text{CO}(2-1)}$ are adjusted to cover 0.7 times the shown range of $I_{\text{CO}(1-0)}$ for a fairer comparison using a (fiducial) average line ratio $I_{\text{CO}(2-1)}/I_{\text{CO}(1-0)}$ of 0.7. The $I_{\text{CO}(1-0)}$ and $I_{\text{CO}(2-1)}$ maps appear similar for prominent structures, although their ratio maps show variations (see Section 4).

4. RESULTS

From the integrated intensity maps in Section 3, we calculated the line ratio $R_{21} \equiv I_{\text{CO}(2-1)}/I_{\text{CO}(1-0)}$ maps (Figures 5-10). We applied a signal-to-noise (SN) cut of >5 in CO(1-0) to ensure enough significance in the denominator of the ratio. While the CO(1-0) sensitivity is similar among all the galaxies, the CO(2-1) sensitiv-

ity varies between galaxies. Hence, we impose a less stringent cut of >3 in CO(2-1) to mitigate the effect of noise.

We summarize the R_{21} values and their distribution for each galaxy individually. The spatial resolutions of our maps at the adopted angular resolution of $2.5''$ range from ~ 50 -200 pc amongst the sample (Table 1), larger than the typical size of a molecular cloud. The R_{21} values presented here thus represent the average R_{21} within individual molecular clouds.

4.1. R_{21} Maps and Distributions

The R_{21} maps for each galaxy and their distributions (histograms), as well as their optical images for comparison, are shown in Figures 5-10. We summarize the R_{21} variations in each galaxy separately (see Table 3). We tend to find similar trends in each morphological type and galactic structure (e.g., barred, unbarred, spiral), which leads us to classify them according to their optical and molecular gas morphologies (Section 5).

We divide the molecular gas using the definitions adopted in Hasegawa (1997, for a review). Low-ratio gas (LRG) have $R_{21} < 0.7$ (blue), high-ratio gas (HRG) are in between $0.7 < R_{21} < 1.0$ (red), and very-high-ratio gas (VHRG) have $R_{21} > 1.0$. The division of molecular gas at $R_{21} = 0.7$ (white) is motivated both theoretically via the LVG approximation (Goldreich & Kwan 1974; Scoville & Solomon 1974) and observationally first in MW studies (e.g., Sakamoto et al. 1997; Oka et al. 1998a; Hasegawa 1997). Typical molecular gas with physical conditions (n_{H_2}, T_k) = (300 cm^{-3} , 10 K) have $R_{21} \sim 0.6$ -0.7 (i.e., LRG), with the transition from LRG to HRG requiring 2-3x denser and/or hotter gas (e.g., Koda et al. 2012). On the other hand, VHRG with $R_{21} > 1.0$ is difficult to achieve, requiring optically thin conditions yet even denser/hotter gas.

The blue and green histograms show how the bulk of the molecular gas in each galaxy are distributed by area (number) and mass (weighted by $I_{\text{CO}(1-0)}$), respectively. They show the overall distribution (lightest shade) and the contribution from the central 1 kpc ($R < 0.5$ kpc, darkest shade) in the plane of each galaxy, following the definition for central regions adopted in e.g. Sakamoto et al. (1999); Sheth et al. (2005). The central 1 kpc has been used as a fiducial value for central regions in the literature. However, the size of the central region depends on the galaxy, and based on the R_{21} maps, the region of HRG in the centers of galaxies can extend beyond $R > 0.5$ kpc. We thus also show the contribution from the central 2 kpc ($R > 1.0$ kpc, hatched, dark shade) in the histograms.

4.1.1. NGC 0628

Table 1. Sample properties of ALMA-FACTS and adopted parameters for the bar. The corresponding spatial resolution at $2.5''$.

Galaxy	Morphology	Distance	D_{25}	Inclination	PA_{disk}	R_{bar}	PA_{bar}	ϵ_{bar}	Scale ($2.5''$)
		[Mpc]	(')	[$^{\circ}$]	[$^{\circ}$]	[']	[$^{\circ}$]		[pc]
(1)	(2)	(3)	(4)	(5)	(6)	(7)	(8)	(9)	(10)
NGC 0628	SAC	9.8 (1)	10.5	19.8	20	—	—	—	119
NGC 1097	SBb	15.4 (2)	9.3	54.8	133.9	95.1	141	0.65	187
NGC 1512	SBa	12.6 (2)	8.9	68.3	65.2	73.5	42	0.66	153
NGC 3351	SBb	9.33 (3)	7.4	54.6	10.7	53.6	112	0.46	113
NGC 3521	SA*	12.1 (2)	11	60.0	162.8	—	—	—	147
NGC 3621	SAd	6.55 (3)	12.3	67.6	161.7	—	—	—	79
NGC 3627	SABb	9.38 (3)	9.1	67.5	168.1	59.1	160	0.76	114
NGC 4254	SAC	13.9 (4)	5.4	20.1	66	—	—	—	168
NGC 4321	SABbc	14.3 (2)	7.4	24.0	158	54.6	108	0.59	173
NGC 4536	SABbc	14.5 (2)	7.6	73.1	120.7	39.8	77	0.50	176
NGC 4579	SABb	16.4 (4)	5.9	41.9	90.2	42.2	53	0.48	199
NGC 4826	SAab	4.41 (5)	10	64.0	114.0	—	—	—	53

NOTE—Columns (2-6) are from Komugi et al. (2025, Paper II).

(1) Galaxy.

(2) Galaxy morphology taken from RC3 (de Vaucouleurs et al. 1991). * For NGC 3521, de Vaucouleurs et al. (1991) lists this as a SABbc galaxy, but is treated as an unbarred SA for reasons explained in Komugi et al. (2025).

(3) Redshift-independent distance. Numbers in parentheses is the reference. In order of preference, measurements taken from Cepheid variables, tip of RGB, Tully-Fischer relation. References : 1. McQuinn et al. (2017), 2. Tully et al. (2016), 3. Freedman et al. (2001), 4. Tully et al. (2013), 5. Anand et al. (2021).

(4) Isophotal diameter at the major axis, taken from RC3 (de Vaucouleurs et al. 1991).

(5)(6) Inclination and position angle taken from HyperLEDA (Makarov et al. 2014) when available, or from Kuno et al. (2007), Sorai et al. (2019).

(7-9) Adopted semi-major axis, position-angle, and ellipticity of the bar from Herrera-Endoqui et al. (2015) for bar region masks (section 5.2.5).

(10) Spatial resolution at $2.5''$.

NGC 0628 is an isolated spiral galaxy (SAC) with many star-forming regions (HII) along its spiral arms. It does not have a bar structure. At its distance, the angular resolution $2.5''$ corresponds to a spatial resolution of 119 pc. From Figure 3, the molecular gas distribution in NGC 0628 is relatively dim in both transitions of CO and its spiral arms appear loosely wound. The stellar spiral arms extend beyond the CO coverage (e.g., Figure 1).

The R_{21} measurements are concentrated around the spiral arms due to the sensitivity limitation, with that in the interarm regions only occasionally determined. The disk is dominated by low-ratio gas (Figure 5), encompassing 70% of the significantly detected pixels, while high-ratio gas makes up 24% (blue histogram). This is similar for the CO(1-0) intensity distribution (green

histogram), with low-ratio gas and high-ratio gas containing 78% and 18% respectively. Over the whole area, the mean R_{21} is 0.62 while the intensity-weighted mean is 0.59.

Barnes et al. (2023) conducted a detailed case-study of the Phantom Void (1 kpc bubble) in this galaxy. They suggested the bubble is sustained by stellar feedback. In Figure 5, the molecular gas around there does not show a particular excess in R_{21} .

4.1.2. NGC 1097

NGC 1097 is a strongly barred, interacting spiral galaxy (SBb). At its distance, the angular resolution of $2.5''$ corresponds to a spatial resolution of 187 pc. It is the second-farthest galaxy in the sample. From Figure 3, the molecular gas distribution shows a prominent central core and offset ridges along the bar. The

spiral arms extend from the bar ends beyond our coverage (e.g., Figure 1). There are also interarm structures (structures between the offset ridges) that often appear filamentary.

R_{21} is high in the center, becomes lower along the bar, and then increases at the bar ends (Figure 5). Low-ratio gas and high-ratio gas make up 73% and 24% of the area (blue histogram), respectively. However, the CO(1-0) intensity contained by low-ratio and high-ratio gas are similar, at 48% and 50% respectively (green histogram). Over the whole area, the mean R_{21} is 0.61 while the intensity-weighted mean is 0.70.

From the dark/hatched and darkest regions in the histograms, the central 1-2 kpc ($R < 1$ kpc) contains mostly high-ratio gas. The middle panel shows a 1-kpc scale (white bar) in the lower-right corner. The high-ratio gas region, and the central gas concentration, in this galaxy extends even beyond the traditional definition of the central 1 kpc region (Sakamoto et al. 1999; Sheth et al. 2005). In any case, the whole region is located at the roots of the offset ridges.

4.1.3. NGC 1512

NGC 1512 is a barred spiral galaxy (SBa) with a companion. At its distance, the angular resolution of $2.5''$ corresponds to a spatial resolution of 153 pc. From Figure 3, the molecular gas distribution in NGC 1512 shows a bright core and two offset ridges. The ridges are significantly detected in their inner parts but not in the outer parts. The CO emission re-appears around the bar ends, which continues to fainter spiral arms.

R_{21} is high in the center and becomes lower along the offset ridges (Figure 6). The R_{21} along the spiral arms fluctuate between low-ratio and high-ratio, with some high-ratio gas spatially coincident with HII regions. This galaxy also has a central gas concentration and high ratio region larger than the nominal definition of the central 1 kpc. Indeed, the histogram for the central 2 kpc explains most of the HRG. Low-ratio and high-ratio gas encompass 58% and 36% of the area shown, respectively. However, low-ratio gas contain 37% of the CO(1-0) intensity, while 56% is contained within the high-ratio gas. Over the whole area, the mean R_{21} is 0.67 while the intensity-weighted mean is 0.76. From the histograms, the central 1-2 kpc ($R < 1.0$ kpc) contain mostly high-ratio gas.

4.1.4. NGC 3351

NGC 3351 is a barred spiral galaxy (SBb). The angular resolution of $2.5''$ corresponds to 113 pc. From Figure 3, the molecular gas distribution in NGC 3351 has a bright central core and two offset ridges, also sur-

rounded by spiral arms. The offset ridges are bright in the inner part of the bar, but not in the outer part.

In Figure 6, R_{21} is high in the center and decreases along the offset ridges, but fluctuates in the surrounding spiral arms between low and high ratios. Low-ratio and high-ratio gas make up 67% and 30% of the area shown (blue histogram). However, the amount of low-ratio gas and high-ratio gas contained by the CO(1-0) intensity are similar at 44% and 55%, respectively (green histogram). Over the whole area, the mean R_{21} is 0.65 while the intensity-weighted mean is 0.73. From the histograms, high-ratio gas is concentrated predominantly in the central kiloparsec ($R < 0.5$ kpc) region.

4.1.5. NGC 3521

NGC 3521 is a spiral galaxy (SA) with star-forming (HII) regions spread across its disk. This is an unbarred galaxy. The resolution of $2.5''$ corresponds to 147 pc. The optical image of NGC 3521 shows a flocculent pattern across the disk, but from Figure 3, the molecular gas distribution shows tightly wound spiral arms. Both transitions of CO are detected across the disk, but there is no central gas concentration as seen in the barred galaxies.

R_{21} fluctuates between low and high values along the spiral arms (Figure 7). Low-ratio and high-ratio encompass 53% and 45% of the disk respectively (blue histogram). The CO(1-0) intensity contained by the low-ratio and high-ratio gas are 50% and 49% respectively (green histogram). Over the whole area, the mean R_{21} is 0.69 while the intensity-weighted mean is 0.70. As both transitions of CO are not detected in the center, there is little contribution from the central kiloparsec ($R < 0.5$ kpc) in the R_{21} distributions, if any.

4.1.6. NGC 3621

NGC 3621 is another isolated unbarred spiral galaxy (SAd) with star-forming regions spread across its disk. At its distance, the angular resolution of $2.5''$ corresponds to a spatial resolution of 79 pc. It is the second-closest galaxy in the sample.

From Figure 3, the molecular gas structure appears less organized and flocculent. R_{21} fluctuates between low and high values across the disk (Figure 7). The spatial distribution of high-ratio gas seems to coincide closely with HII regions. Low-ratio gas and high-ratio gas cover 36% and 57% of the area shown (blue histogram). The CO(1-0) intensity contained by low-ratio and high-ratio gas are 27% and 67% (green histogram). Hence, the majority of the molecular gas by area and by CO(1-0) intensity have high-ratios. Over the whole area, the mean R_{21} is 0.75 while the intensity-weighted mean is 0.78.

4.1.7. *NGC 3627*

NGC 3627 is an interacting barred spiral galaxy (SABb) in the Leo Triplet group. At its distance, the angular resolution of $2.5''$ corresponds to a spatial resolution of 114 pc. From Figure 4, the molecular gas distribution in NGC 3627 shows a prominent center and bar, with coherent spiral arms extending from the bar ends. The central region and bar ends are bright in both CO transitions.

R_{21} is high in the center, lowers along the bar, and then increases again at the bar ends (Figure 8). The high ratio regions especially at the bar ends and along the spiral arms are located near the HII regions in the optical image. Low-ratio and high-ratio gas encompass 59% and 36% of the galaxy by area (blue histogram), while they contain a similar amount of the CO(1-0) intensity at 49% and 49% (green histogram), respectively. Over the whole area, the mean R_{21} is 0.68 while the intensity-weighted mean is 0.71. The majority of the gas in the central kiloparsec ($R < 0.5$ kpc) is high-ratio gas.

den Brok et al. (2023) also studied R_{21} in NGC 3627 (as well as other line ratios including CO(3-2) ALMA observations) at $4''$ resolution (~ 200 pc). They also found high R_{21} in the center and bar-ends, in comparison to the bar and spiral arms.

4.1.8. *NGC 4254*

NGC 4254 is an interacting spiral galaxy (SAc) in the Virgo cluster. The angular resolution of $2.5''$ is 168 pc. From Figure 4, the molecular gas distribution appears asymmetric (e.g., Hidaka & Sofue 2002). The center is bright and spiral arms are apparent in both transitions of CO, but the structures of the spiral arm and tightness differ between the northern and southern parts. The southern spiral arm extends beyond the coverage in CO (e.g., Figure 1).

R_{21} fluctuates between low and high-values along the spiral arms in the disk. Low-ratio and high-ratio gas encompass 52% and 44% of the area (blue histogram). Low-ratio and high-ratio gas include similar portions of the CO(1-0) intensity distribution, at 46% and 52% respectively (green histogram). Over the whole area, the mean R_{21} is 0.69 while the intensity-weighted mean is 0.71. From the histogram, the central kiloparsec ($R < 0.5$ kpc) contains mostly high-ratio gas.

4.1.9. *NGC 4321*

NGC 4321 is a barred spiral galaxy (SABbc). The $2.5''$ resolution corresponds to 173 pc. From Figure 4, the molecular gas distribution shows a bright center and two spiral arms in both CO transitions. The spiral arms extend beyond the CO coverage (e.g., Figure 1).

We note that for NGC 4321, the sensitivity in the CO(2-1) data between the northern and southern parts of the galaxy differs by about a factor of two (Figure 2). However, the analysis of the center, bar, and bar ends are all in the southern part where the sensitivity is better. Thus, we discuss the structural variations of R_{21} in this galaxy as we do in the other galaxies.

R_{21} is high in the center, lowers in the bar region, but fluctuates between low and high-values along the spiral arms (Figure 9). The southern spiral arm may be showing a potential transition from low to high-ratio gas along the gas flow across the spiral arm (where it runs horizontally in the image), assuming that the gas passes through the arm in the counter-clockwise direction. Low-ratio gas encompasses 63% of the disk while high-ratio gas makes up 30% by area (blue histogram). Likewise, low-ratio gas contains 55% of the CO(1-0) intensity and high-ratio gas contains 39% (green histogram). Most of the molecular gas distribution in NGC 4321 thus has low-ratios by area and by CO(1-0) intensity. Over the whole area, the mean R_{21} is 0.64 while the intensity-weighted mean is 0.67. The central 1-2 kpc is mostly high ratio gas.

4.1.10. *NGC 4536*

NGC 4536 is a barred spiral galaxy (SABbc). At its distance, the angular resolution of $2.5''$ corresponds to a spatial resolution of 176 pc. From Figure 4, the center is bright in both CO transitions and has two spiral arms which extend beyond the CO coverage (e.g., Figure 1). The bar is likely running nearly along the minor axis of the disk (Díaz-García et al. 2016), but because the bar appears substantially shorter due to this projection, its orientation can be debated (Mazzalay et al. 2014).

R_{21} is high in the center but fluctuates between low and high-values along the spiral arms (Figure 9). The peak of the R_{21} distribution by number is in low-ratio gas (blue histogram), but the peak shifts to high-ratio gas when weighted by CO(1-0) intensity (green histogram). Low-ratio gas and high-ratio gas encompass 70% and 27% of the area. However, low-ratio gas contains 32% of the CO(1-0) intensity distribution, with high-ratio gas containing 52%. Over the whole area, the mean R_{21} is 0.61 while the intensity-weighted mean is 0.79. From the histograms, there is molecular gas concentrated in the central region, with the central 1-2 kpc containing predominantly high/very-high ratio gas.

4.1.11. *NGC 4579*

NGC 4579 is a barred spiral galaxy (SABb). At its distance, the angular resolution of $2.5''$ corresponds to a spatial resolution of 199 pc. It is the farthest galaxy in the sample. From Figure 4 the central region is bright in

both CO transitions and is surrounded by spiral arms. There is a concentration of gas in the central region. Its structure is spatially resolved and in the CO(1-0) map, it also looks like the roots of offset ridges. We treat it as a central concentration but since the transition from a central concentration to offset ridges is continuous, the boundary cannot be defined clearly.

R_{21} is high in the center. The central gas concentration and high ratio region is also larger than the nominal definition of the central 1 kpc. Indeed, the histogram for the central 2 kpc explains most of the HRG. R_{21} appears to fluctuate along the spiral structure (Figure 10). The distribution of the R_{21} in the histogram weighted by CO(1-0) intensity appears doubly-peaked, signifying the difference in the R_{21} distributions between the central region and spiral arms structure. The peaks of the distributions by number and when weighted by CO(1-0) are both in low-ratio gas. Low-ratio gas and high-ratio gas encompass 88% and 10% of the area, respectively (blue histogram). However low-ratio gas contains 74% of the CO(1-0) intensity while high-ratio gas contains 16%. Over the whole area, the mean R_{21} is 0.53 while the intensity-weighted mean is 0.62. From the histograms, the central 1-2 kpc contains mostly high/very-high ratio gas, while the spiral arms contain low-ratio gas.

4.1.12. NGC 4826

5. DISCUSSION

This work presents high-resolution R_{21} maps of a sample of nearby spiral galaxies, an early result from the ALMA-FACTS survey. While we plan on more quantitative analyses in our subsequent papers, the R_{21} maps already offer the first opportunity to compare the variations of R_{21} amongst galaxies. The R_{21} maps appear to show some general trends with respect to galactic morphology. While discussions on morphology tend to be empirical, we attempt to characterize the general trends in terms of galactic structures. In particular, the galactic centers, bars, and spiral arms appear to play their own distinct roles in the organization of the molecular gas conditions traced by R_{21} , in addition to their mass distributions as often discussed in the literature. These empirical characterizations also seem consistent with the results in recent case studies (e.g., den Brok et al. 2021; Egusa et al. 2022; Maeda et al. 2022; den Brok et al. 2023).

We will first explain an idea for the stellar and gas morphology-based classifications and supporting dynamical models in the literature (section 5.1). We then

NGC 4826 is an unbarred spiral galaxy (SAab). At its distance, the angular resolution of $2.5''$ corresponds to a spatial resolution of 53 pc. It is the closest galaxy in the sample. The CO coverage of this galaxy in linear size is around the size of the central regions of the other galaxies in the sample. The molecular gas properties presented thus may be more comparable to the centers of galaxies. From Figure 4, this central region is prominent and bright in both CO transitions.

R_{21} is high in the center but fluctuates between low and high in the surrounding regions. Low-ratio and high-ratio gas comprise similar portions of the galaxy by area, at 48% and 49% respectively. However, low-ratio gas contains 36% of the CO(1-0) intensity, while high-ratio gas contains 56%. Over the whole area, the mean R_{21} is 0.71 while the intensity-weighted mean is 0.76. Given the small linear extent of the molecular gas, this skewed distribution towards high-ratio gas may be consistent with those in the central regions of the other galaxies, especially in the barred galaxies (see Figure 13). This might indicate that once the gas is concentrated in the central regions, R_{21} becomes high independent of the cause of the concentration.

discuss the behaviors of R_{21} in the galactic centers, bars, bar ends, and spiral arms, as well as radial and azimuthal variations of R_{21} along this empirical classification (section 5.2).

5.1. Morphology-Based Classification

For characterizing general trends in R_{21} , we rearrange the sample galaxies based on (1) their optical morphologies and (2) molecular gas morphologies (i.e., molecular gas distributions) with emphasis on bar and spiral arm structures. Their optical morphologies are classified as barred (SB and SAB) and unbarred spiral galaxies (SA), which appear to primarily determine the behaviors of R_{21} across the disks. For barred galaxies, there is a suggested picture on the gas evolutionary sequence based on hydrodynamical simulations and observations (Sakamoto et al. 1999; Sheth et al. 2005; Yu et al. 2022), which appears to help understand the behaviors of R_{21} amongst the barred galaxies. We summarize this evolutionary sequence and discuss our arrangement of the sample galaxies.

5.1.1. Bar-Driven Gas Transport

In the bar-driven gas transport model, the stellar bar potential organizes the gas motions to form the offset

Table 2. CO(2-1) and CO(1-0) 12m+07m+TP data cube parameters before and after smoothing to 2.5'' angular resolution. The listed RMS noises are measured in high-sensitivity regions of emission-free channels.

(1)	(2)	(3)	(4)	(5)
Galaxy	FoV	Beam Size	RMS Noise (1 σ)	
	Map Area, P.A.	b _{maj} , b _{min} , P.A.	Native Res.	Smoothed (2.5'')
	[$' \times ', ^\circ$]	[$'' , '' , ^\circ$]	[mK]	[mK]
CO(2-1) Data Cube Parameters				
NGC 0628	4.3 \times 2.9, 135	1.48, 0.88, -61.04	74.9	24.9
NGC 1097	4.4 \times 2.5, 145	1.54, 1.17, -85.48	46.2	18.5
NGC 1512	3.1 \times 2.2, 37	1.23, 0.99, 85.14	71.9	21.8
NGC 3351	2.6 \times 2.5, 0	1.44, 1.20, -78.83	92.2	36.2
NGC 3521	4.9 \times 2.1, 160	1.39, 1.12, -81.01	37.9	13.6
NGC 3621	4.2 \times 2.3, 160	1.55, 1.13, -79.09	31.8	12.2
NGC 3627	4.2 \times 2.3, 0	1.16, 1.00, 44.23	92.0	28.1
NGC 4254	3.5 \times 3.0, 0	1.64, 1.17, 57.54	53.1	22.4
NGC 4321	3.6 \times 3.1, 90	1.13, 1.00, -30.25	102.5	28.5
NGC 4536	4.2 \times 1.8, 119	1.55, 1.22, -71.86	25.3	10.0
NGC 4579	3.0 \times 2.2, 52	1.52, 1.33, -73.31	39.3	16.8
NGC 4826	2.8 \times 1.8, 112	1.35, 1.18, -23.85	53.6	19.1
CO(1-0) Data Cube Parameters				
NGC 0628	4.3 \times 3.3, 135	2.42, 1.94, -56.77	63.8	49.0
NGC 1097	4.8 \times 2.8, 145	2.11, 1.69, 89.44	75.7	47.4
NGC 1512	3.1 \times 2.5, 37	2.24, 1.70, 88.36	60.6	39.9
NGC 3351	2.9 \times 2.8, 0	2.10, 2.02, -72.57	60.0	42.0
NGC 3521	5.3 \times 2.5, 160	2.18, 1.95, 88.84	67.1	47.5
NGC 3621	4.4 \times 2.9, 160	2.16, 1.64, 84.68	75.5	47.0
NGC 3627	4.4 \times 2.9, 0	2.17, 2.08, -46.96	68.8	50.4
NGC 4254	4.0 \times 3.7, 0	2.41, 1.95, -49.85	68.9	52.8
NGC 4321	4.0 \times 3.6, 90	2.17, 1.95, -58.89	68.7	48.2
NGC 4536	4.5 \times 2.2, 119	2.10, 2.01, 85.63	59.2	41.3
NGC 4579	3.1 \times 2.6, 52	2.20, 1.93, -51.86	74.0	52.2
NGC 4826	3.1 \times 2.1, 112	2.45, 2.02, -22.37	55.1	44.4

NOTE— (1) Galaxy (2) Rectangular field-of-view (FoV) enclosing the region out to where the sensitivity drops to 50% of the peak sensitivity (40% for NGC 4321 CO(2-1)). The position angle (PA) is along the major axis of the map, counterclockwise from North. (3) Beam Size. (4)(5) RMS Noise for the 12m+07m+TP data in 5 km/s channel at the native and smoothed resolutions, respectively.

ridges on the leading side of the bar. The interactions between the gas along the offset ridges (e.g., shocks) and/or with the stellar potential (e.g., torque) cause the gas to lose angular momentum, and the gas falls towards the center from the offset ridges (Wada 1994; Sheth et al. 2002). This picture is supported by observations by Sakamoto et al. (1999) and Sheth et al. (2005). They studied the central regions of barred spiral

galaxies, and found that the central kiloparsec of barred spiral galaxies have higher concentrations of molecular gas than their unbarred counterparts. They attributed the concentrations of molecular gas in their central regions to the bar-driven gas transport by stellar bars to the centers.

5.1.2. Classification

Table 3. Area and intensity-weighted R_{21} , and the molecular gas surface density within and outside of the fiducial 1 kpc central region.

(1)	(2)	(3)	(4)	(5)	(6)	(7)	(8)	(9)
Galaxy	$\Sigma_{\text{H}_2}^{\text{center}}$	$\Sigma_{\text{H}_2}^{\text{outside}}$	R_{21} by Area			R_{21} by I_{CO}		
	$[\text{M}_{\odot} \text{ pc}^{-2}]$	$[\text{M}_{\odot} \text{ pc}^{-2}]$	Mean	LRG [%]	HRG [%]	Mean	LRG [%]	HRG [%]
NGC0628	40	34	0.62	70	24	0.59	78	18
NGC1097	647	71	0.61	73	24	0.70	48	50
NGC1512	61	12	0.67	58	36	0.76	37	56
NGC3351	319	18	0.65	67	30	0.73	44	55
NGC3521	24	40	0.69	53	45	0.70	50	49
NGC3621	21	16	0.75	36	57	0.78	27	67
NGC3627	383	39	0.68	59	36	0.71	49	49
NGC4254	266	65	0.69	52	44	0.71	46	52
NGC4321	490	67	0.64	63	30	0.67	55	39
NGC4536	403	19	0.61	70	27	0.79	32	52
NGC4579	240	30	0.53	88	10	0.62	74	16
NGC4826	200	61	0.71	48	49	0.76	36	56

NOTE—

(1) Galaxy.

(2) Average molecular gas surface density within the central 1 kpc using $\alpha_{\text{CO}}=4.35$ in each galaxy.

(3) Same as (2) but outside of the central 1 kpc.

(4-6) Mean R_{21} , and percentage of molecular gas in LRG and HRG across the whole area of the galaxy.(7-9) Same as (4-6) but weighted by $I_{\text{CO}(1-0)}$.

Figure 11 shows the R_{21} maps from Section 4 arranged primarily by their optical morphological classifications (SB, SAB, or SA), and secondarily by their gas morphology for the barred galaxies. The secondary part is based on the presence or absence of gas along the offset ridges. Even when the offset ridges are not present, all of the barred galaxies have central condensations of gas, and thus fit within the bar-driven gas transport picture, if the absence of the ridges is due to the gas inflow. Hence, using the optical and gas morphological classifications, we arrange the R_{21} maps (ordered by galaxy number) starting from barred galaxies with shorter offset ridges, i.e., lacking molecular gas between the central region and spiral arms, to barred galaxies with longer offset ridges and having clearer spiral arms extending from the bar ends, and then to the unbarred galaxies.

In the arranged evolutionary sequence of Figure 11, the barred galaxies NGC 1512, NGC 3351, NGC4579, and NGC 4536 (top row) have shorter offset ridges and/or show an absence of gas between the central regions and their surrounding spiral arm structures. Following these, the barred galaxies NGC 1097, NGC 3627, and NGC 4321 (left middle row) show longer offset ridges and have clearer spiral arms extending out of the

bar ends. The rest of the galaxies are unbarred (the bottom row and the rightmost in the middle row). Figure 13 is the same as Figure 11, but shows the galaxies on the same physical scale. NGC 4826 (unbarred) is placed succeeding the barred galaxies (middle row) since it has a central gas condensation/region with a linear size more comparable to those of the barred galaxies (e.g., Section 4.1 and Figure 13).

In Table 3, we include the derived average molecular gas surface densities from $I_{\text{CO}(1-0)}$ within ($\Sigma_{\text{H}_2}^{\text{center}}$) and outside ($\Sigma_{\text{H}_2}^{\text{outside}}$) of the fiducial 1 kpc central region. We assume the Milky-Way $\alpha_{\text{CO}} = 4.35 \text{ M}_{\odot} \text{ pc}^{-2} \cdot [\text{K} \cdot \text{km} \cdot \text{s}^{-1}]^{-1}$ value (Bolatto et al. 2013). The $\Sigma_{\text{H}_2}^{\text{center}}$ are consistent with Sakamoto et al. (1999) and Sheth et al. (2005) for common galaxies after accounting for differences in the adopted CO-to-H₂ conversion factor and observational uncertainties. Amongst the barred galaxies, those with longer offset ridges have overall higher molecular gas surface densities in the central 1 kpc region and the rest of the disk than those with shorter offset ridges.

In the following sections, we discuss R_{21} along this sequence to understand the observed trends in R_{21} as a function of structure.

5.2. Structural Dependence of R_{21}

We discuss the overall trends in R_{21} seen amongst the barred and unbarred galaxies, and then within each galactic structure (center, bar, bar ends, and spiral arms). Figure 12 shows the radial distributions (each pixel) of R_{21} , in the same arrangement as Figure 11. The binned means are shown in red and the secondary x-axis (top) is in arcseconds.

Overall, the barred galaxies (top and left middle rows) follow a general trend: R_{21} is high in the center ($R_{21} \sim 1.0$), low along the bar ($R_{21} \sim 0.6 - 0.7$), increases at the bar ends ($R_{21} \gtrsim 0.7$), and then gradually declines to lower R_{21} towards the disk outskirts, with fluctuations in the spiral arms. The radial distributions of R_{21} in the unbarred galaxies (right middle and bottom rows) look similar to the outer parts of the barred galaxies (Komugi et al. 2025).

There are also some variations in the azimuthal direction in the sample galaxies. However, due to the sensitivity limitations, the interarm regions of the galaxies are not readily detected (Figure 11). Variations in the azimuthal direction can be seen as scatters at each radius in the radial distributions. With these trends in mind, we discuss R_{21} as a function of structure in the following sections.

5.2.1. Central Regions: High R_{21}

It has been known that barred galaxies often have high gas concentrations in their central regions (Sakamoto et al. 1999; Sheth et al. 2005; Yu et al. 2022). The same central gas concentrations are apparent in the barred galaxies in our observations (Figures 3-4). In addition, the sample of the unbarred spiral galaxies do not show such gas concentrations at the centers besides NGC 4826. This study (section 4.1) shows that the central 1-2 kiloparsec regions within barred galaxies also comprise of high/very-high ratio gas, and that the gas physical conditions change within the central gas condensations. The elevated line-ratios in their galactic centers are clear in the radial distributions.

The presence of high-ratio gas across these central regions indicates that the molecular gas there has higher n_{H_2} and T_{k} and is thus denser and/or warmer than the typical molecular gas conditions, $(n_{\text{H}_2}, T_{\text{k}}) = (300 \text{ cm}^{-3}, 10 \text{ K})$, in the disks.

The high ratios may be the result of dynamical processes and/or on-going star formation in the galaxy centers. As a dynamical process, the high ratios in the central regions of the barred galaxies across the sample could be due to the bar-driven gas transport to the centers, discussed in section 5.1.1. The influence of the bar may compress the gas (increase in gas density) and/or

trigger star formation in galactic centers (increase in gas kinetic temperature by stellar feedback) and lead to the high-ratios. The enhancement of star formation in the centers of barred galaxies has been studied e.g., in Ho et al. (1997).

Amongst the sample galaxies, NGC1097, NGC3627, NGC4579, and NGC4826 (as well as NGC 3621) are classified as having AGN (Véron-Cetty & Véron 2010) and this may also be a cause of the high R_{21} there. However, even the galaxies without AGN often show high R_{21} in the central $\sim 1 - 2 \text{ kpc}$ when they have the central gas concentrations. Thus, AGN may not be the only cause of high R_{21} in central regions.

It may also be worth noting that NGC 4826 is an unbarred spiral galaxy in the optical classification, but has a central concentration of high-ratio gas. Although it is only one case, its presence may indicate that the high ratio is due to the local environment of the central region (e.g., strong shears or tidal forces), rather than the compression due to the infalling gas.

5.2.2. Along the Bar: Low R_{21}

Bar regions overall show lower R_{21} ($R_{21} \sim 0.6$). This is evident in the spatial and radial distributions of R_{21} (Figures 11-12), even though there is molecular gas concentrated along the offset ridges and bar (Figures 3-4). This seems to be a general trend amongst barred spiral galaxies, including the ones in other studies: NGC 1300, NGC 1365, NGC 2903, NGC 3627, and NGC 5236 (M83) (Maeda et al. 2022; Egusa et al. 2022; den Brok et al. 2023; Koda et al. 2025). The low R_{21} in the bar region is seen even when the offset ridges do not have much gas (NGC 1512, NGC 3351, and NGC 4579; top row in Figures 11-12).

The lower $R_{21/10}$ suggests that n_{H_2} and T_{k} remain low in the bar, even when the gas is concentrated along the offset ridges. This may explain why star formation efficiency is often low in the bar regions of galaxies (e.g., Downes et al. 1996; Koda & Sofue 2006; Momose et al. 2010; Maeda et al. 2023). Recently, Rodríguez et al. (2024) analyzed the $3.3 \mu\text{m}$ polycyclic aromatic hydrocarbon (PAH) emission in 19 nearby star-forming galaxies to identify star clusters in their early dust-embedded phases. They also found that, in general, there is an absence of PAH emitters in bars (including our FACTS sample: NGC 1512, NGC 3351, NGC 3627, and NGC 4321).

The generally low R_{21} along the offset ridges may also be important in considering gas dynamics within the bar. It has been suggested that the offset ridges are regions of strong shocks (Athanasoula 1992a,b; Sellwood & Wilkinson 1993), which should naturally increase n_{H_2}

and T_k , and hence, R_{21} . Instead, the gas concentration along the offset ridges may be caused by the mere crowding of gas orbits with only occasional collisions (Wada 1994; Koda & Sofue 2006), which could keep R_{21} low in general. In the case of orbit crowding, the gas falls towards the center by the loss of angular momentum due to the gravitational torque of the stellar bar potential, as the gas resides longer on the leading side of the bar. This gas infall process takes longer than the rapid gas transport due to the strong shocks. In addition to explaining the low R_{21} along the bar, this cloud-orbit model may also explain the frequency of offset ridges in the sample of barred galaxies; along the evolutionary sequence, the presence and frequency of the offset ridges (from long to short to none) may imply the molecular offset ridges should last long (Section 5.1.1).

5.2.3. Bar Ends: High R_{21}

Bar ends are the transition regions from the offset ridges in the bar to spiral arms outside the bar. The gas often builds up around the bar ends (e.g., NGC 1097 and NGC 3627 in Figures 11-12, see also Sheth et al. 2002). Even when the offset ridges fade away at their further ends, the CO emission often starts to re-appear around the bar ends and extends along the spiral arms (e.g., NGC 1512, NGC 3351). Star formation is likewise evident at the bar ends in the optical images e.g. for NGC 1097 and NGC 3627 (Figures 5 and 8). Rodríguez et al. (2024) show there is a clustering of $3.3 \mu\text{m}$ PAH emitters at the bar ends of NGC 3627.

The bar ends also show higher R_{21} spatially and in the radial distributions ($R_{21} \gtrsim 0.7$) (Figures 11-12). The high ratios again suggest that the molecular gas located there has relatively higher n_{H_2} and/or T_k .

The stellar bar pattern should have a constant pattern speed to maintain its linear structure over time. The bar end is often considered to be around the co-rotation radius where the orbital speed of gas and stars are synchronized with the bar pattern speed (it is at $\sim 80\%$ of the co-rotation radius according to Athanassoula (1992a,b)). Once the gas gets into the bar end, it will likely reside there for a long time. This explains the gas concentrations around the bar ends. The combination of the high gas concentration and long residential time may trigger local gravitational collapses, which may explain the high R_{21} and star formation (e.g., Maeda et al. 2025). This is, of course, a hypothesis and needs to be verified by future observational and theoretical studies.

5.2.4. Spiral Arms

Spiral arms are also where the gas builds up. R_{21} fluctuates between low and high values along the molecular gas spiral arms (Figures 11-12). It is remarkable that

the fluctuations appear similar between the spiral arms in the barred galaxies and those of the unbarred galaxies. Most of the high-ratio gas in these regions appear to be associated with HII regions, and thus, star formation. This has been found in Galactic and extragalactic studies (e.g., Sakamoto et al. 1994; Seta et al. 1998; Koda et al. 2012, 2020; Egusa et al. 2022; Koda et al. 2025).

These spatial correlations provide an important benchmark for understanding the interplay between molecular gas evolution and star formation in spiral galaxies. However, their causality needs to be discussed with more detailed comparisons with multi-wavelength data or with future observations. In fact, the galactic potential, such as the spiral arm potential, can control gas dynamics/flows, which can compress the gas, increase R_{21} , and trigger star formation. On the other hand, the galactic structures can help in assembling the gas to form stars, and their feedback can increase R_{21} .

In the analysis of the nearby barred spiral galaxy M83, which had higher resolution and sensitivity, Koda et al. (2025) recently found that R_{21} changes systematically from a low ratio in the interarm regions to high ratio in the bar and spiral arms even without star formation. They concluded that the large-scale galactic dynamics plays an important role in the evolution of molecular gas, in addition to the local impacts of stellar feedback. Indeed, within the spiral arms of NGC 4321, R_{21} appears to change from low to high, when comparing one side of the arm to the other. This may also apply to NGC 1097 and NGC 3627.

5.2.5. R_{21} by Structure

R_{21} clearly varies within each galaxy. The dependence on galactic structures (center, bar, bar ends, and spiral arms) is apparent in Section 4.1. For a more quantitative comparison, we define regions to enclose the structures in each galaxy (Figure 11). We created masks for the center, bar, and bar ends. Our adopted region definitions are not meant to be exact boundaries, but are an attempt to capture the rough areas of the structures of interest. We describe the definitions and R_{21} distribution in each region below.

For the central regions, we adopt either 1 or 2 kpc diameter areas around the galactic center (projected in the sky). We adopt the fiducial 1 kpc for all *unbarred* galaxies. For the *barred* galaxies, we showed that the size of the high-ratio region in the center sometimes extends beyond this in section 4.1. We adopt 2 kpc for all barred galaxies except for NGC3351 and NGC3627.

For the bar and bar ends, we define regions based on the cataloged bar structure (cyan ellipse) in Herrera-Endoqui et al. (2015), which is based on Spitzer $3.6 \mu\text{m}$

from S4G (Sheth et al. 2010; S4G Team 2020). We use their on-sky PA_{bar} , semi-major axis R_{bar} , and ellipticity (see Table 1). The bar region is enclosed by the cyan ellipse but does not include the bar ends (magenta). The bar ends are 2 kpc circles centered on the “tips” of the ellipse. We adopt the definitions of the spiral arms from Querejeta et al. (2021). The area outside the center, bar, bar end, and spiral arms is analyzed as interarm regions.

Figure 14 shows the R_{21} distributions based on these definitions. They reflect the general trends discussed in section 5.2. Central regions of barred galaxies show high $R_{21} > 0.7$. Bars show mostly low $R_{21} < 0.7$. Bar ends for the galaxies with relatively gas-rich offset ridges typically show high $R_{21} > 0.7$. The other galaxies with gas-poor offset ridges lack the gas to be measured, or tend to exhibit lower ratios than those of the gas-rich barred galaxies. Interarm regions contain mostly low-ratio gas and show overall lower R_{21} than the spiral arms.

We note that Querejeta et al. (2021) also defined the inner structures (the center, bar, and bar ends). Their bar ends are defined as overlap regions of bar and spiral arms, but are not identified when their bar is defined too short to reach the spiral arms. This does not assure a consistent analysis across the galaxy sample, and thus, we adopted the above definitions. The trends of R_{21} discussed above for the centers and bars are the same when we use their definitions.

6. SYSTEMATIC TRENDS AND COMPARISON TO LITERATURE

In sections 4 and 5, we showed that R_{21} systematically varies as a function of galactic structure in the twelve nearby spiral galaxies. Such structural variations were not previously clear from single-dish surveys (den Brok et al. 2021; Yajima et al. 2021; Leroy et al. 2022). Komugi et al. (2025, Paper II) conducted the R_{21} analysis using the ALMA-TP component only. They were not able to resolve the galactic structures with their coarser resolution, but found that most of the barred galaxies showed steeper radial gradients, whereas all the unbarred galaxies showed flat or shallower gradients.

This general trend of structure-dependent variations is consistent with the results from high-resolution ALMA case studies. For example, Egusa et al. (2022) studied NGC1365 at ~ 200 pc resolution and found high $R_{21} > 0.7$ in the center while it is low $R_{21} < 0.7$ in the bar region. Maeda et al. (2022) studied NGC1300 at ~ 100 pc resolution, finding R_{21} to be low along the bar ~ 0.50 , high ~ 0.72 in the bar end, and ~ 0.60 in the spiral arm. While these studies covered only small regions within in-

dividual galaxies, the results are consistent with the general trend. Furthermore, den Brok et al. (2023) studied R_{21} in the disk of NGC3627 at ~ 200 pc resolution and found a consistent trend, with high $R_{21} \sim 0.90$ in the center, low ~ 0.70 along the bar, and then increasing again at the bar ends to ~ 0.86 , and high ~ 0.75 in the spiral arms. The same trend was also found in M83 at a higher 46 pc resolution (Koda et al. 2025). The high R_{21} in the centers of the barred galaxies could explain the steeper radial gradients found by Komugi et al. (2025).

Most of these studies, including FACTS, have insufficient sensitivity to detect interarm emission; but when it is detected, it appears to have low-ratios. The M83 study by Koda et al. (2025) has higher sensitivity to detect faint interarm gas, which clearly exhibits low-ratios. As the trends amongst bright structures in M83 is similar to that of the FACTS galaxies and other high-resolution case-studies, we conclude that the observed trends in R_{21} are common amongst all nearby (barred) star-forming spiral galaxies.

7. SUMMARY

In this study, we analyzed the CO(2-1)/CO(1-0) line ratio in twelve nearby galaxies from the Fundamental CO(1-0) Transition Survey (FACTS) in conjunction with the PHANGS CO(2-1) survey. We focused on empirical trends and showed that R_{21} systematically varies as a function of galactic structures in twelve nearby galaxies. To characterize the observed structural variations, we made empirical classifications of the galaxies based on their optical morphologies (SB, SAB, or SA), and their molecular gas morphologies for the barred galaxies, depending on the presence or absence of molecular offset ridges. The molecular gas morphological sequence may be explained as an evolutionary sequence by the bar-driven gas transport model. We discussed R_{21} in the context of this sequence.

From the radial distributions of R_{21} , the barred galaxies follow a general trend: R_{21} is high in the central 1-2 kpc regions ~ 1.0 , low along the bar offset ridges ~ 0.6 , increases at the bar ends $\gtrsim 0.7$, and then declines in the rest of the disk with fluctuations along the spiral arms. The radial distributions of the unbarred galaxies fluctuate in R_{21} and are similar to the outer parts (spiral arms) of the barred galaxies.

High R_{21} in the central 1-2 kpc regions is always associated with the central gas condensations in the barred galaxies. NGC4826 is the only unbarred spiral galaxy in our sample that shows the central condensation and high R_{21} . Low R_{21} along the bar offset ridges suggest that the gas density and/or temperature are lower there, which may explain the reduced star formation efficiency

along bar suggested by previous studies. Bar ends show high R_{21} , indicating increased density and/or temperature. In spiral arms, R_{21} fluctuates. A part of this fluctuation is due to high-ratio gas around HII regions and thus due to star-formation activity, while an impact of galactic dynamics is another possible factor yet to be quantified.

The R_{21} variations found in this study are consistent with previous high-resolution ALMA case studies (NGC 1300, NGC 1365, NGC 3627, and M83). In particular, while interarm emission is not well-detected in this study due to the sensitivity limitation, all the other structures show trends in R_{21} similar to that observed in a recent case-study of M83 which had higher sensitivity and resolution (Koda et al. 2025). The common trends in R_{21} amongst the FACTS sample, M83, and a few other barred galaxies suggests that they may be common amongst all nearby (barred) star-forming galaxies.

We have shown that the variations in R_{21} appear to depend on the galactic structures (the central regions, bar offset ridges, bar ends, and spiral arms). The structure dependence may also suggest the importance of galactic dynamics on the molecular gas evolution and star formation. We plan more detailed multi-wavelength comparisons in our future publications from the FACTS survey.

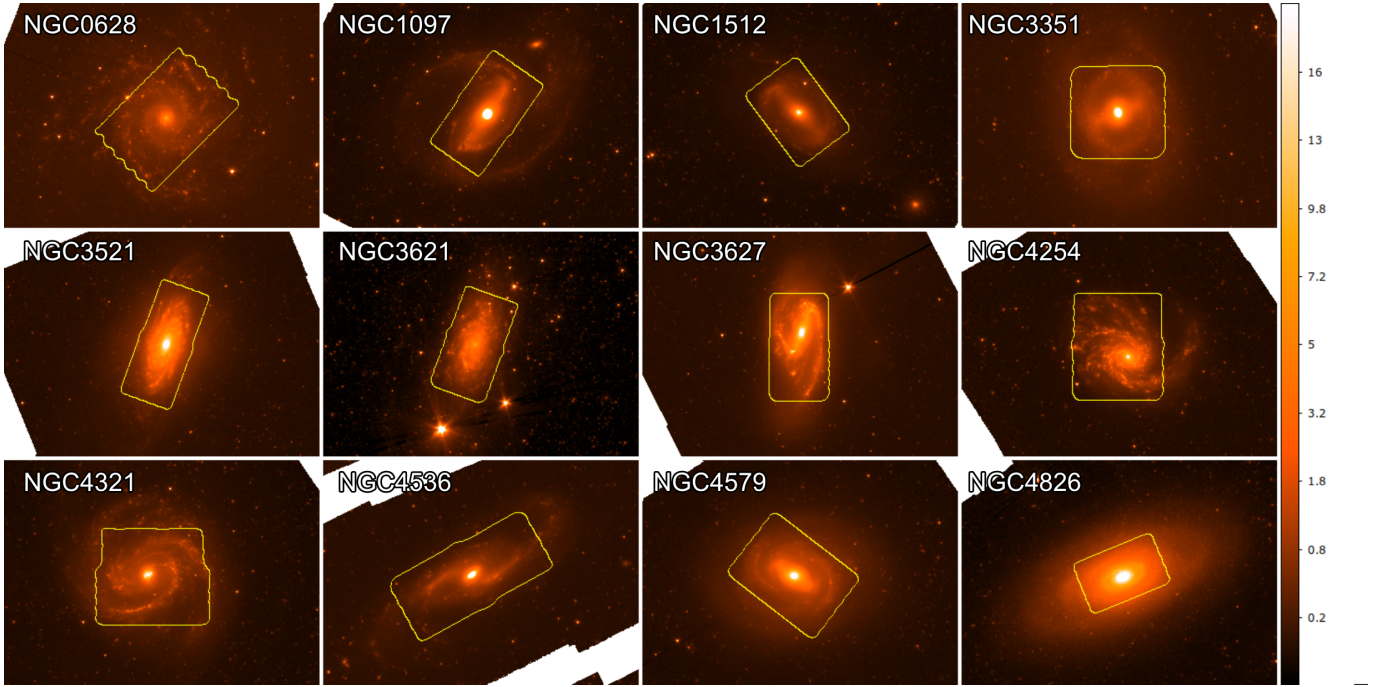


Figure 1. The sample shown in *Spitzer* 3.6 μm emission [MJy/sr] from [Kennicutt et al. \(2003\)](#); [Sheth et al. \(2010\)](#); [S4G Team \(2020\)](#); [SINGS Team \(2020\)](#) to demonstrate the field-of-view (FoV) of the 12m+07m CO(2-1) observations which are overlaid as yellow contours.

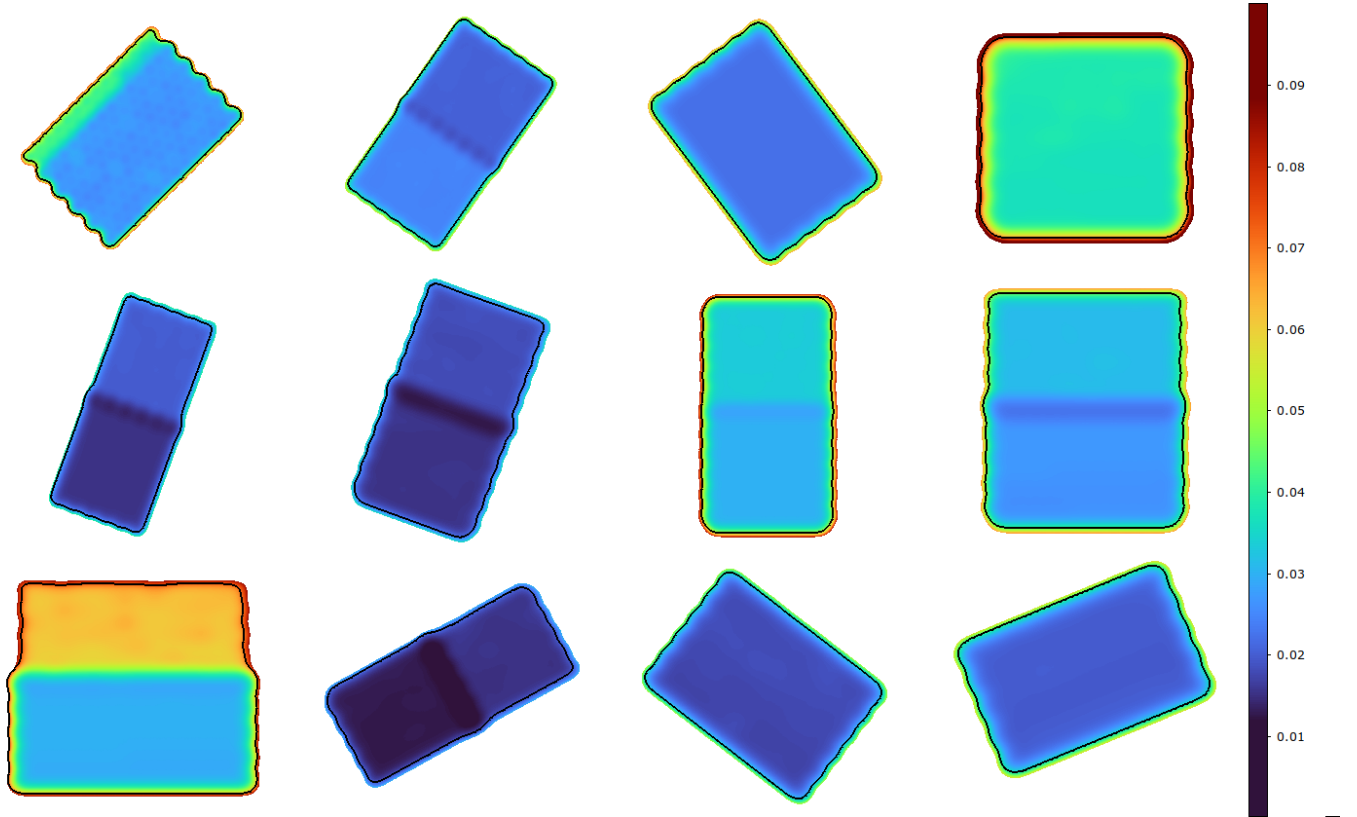


Figure 2. RMS [K] maps for 12m+07m+TP CO(2-1) (measured at the smoothed $2.5''$ resolution) incorporating the sensitivity variations within each galaxy. They are in the same arrangement as Figure 1. The black contours correspond to when the sensitivities drops to $1/2 \sim 50\%$ (40% for NGC4321) of the peak sensitivity of each pointing.

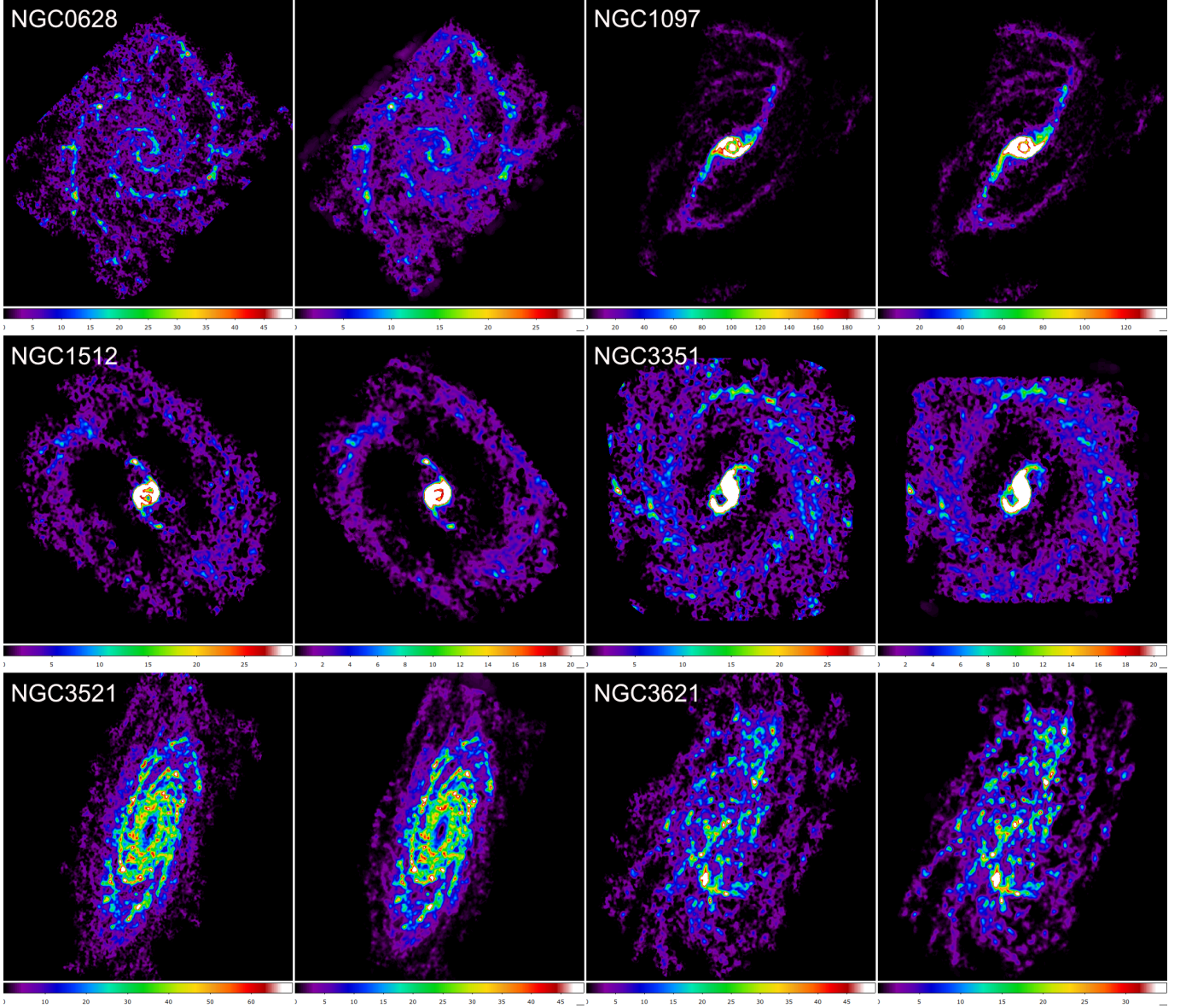


Figure 3. CO(1-0) (left) and CO(2-1) (right) integrated intensity maps [$\text{K}\cdot\text{km}\cdot\text{s}^{-1}$] both at $2.5''$ resolution for NGC0628, NGC1097, NGC1512, NGC3351, NGC3521, and NGC3621 as labeled. The colorbar scale for CO(2-1) is adjusted so that the range covers 0.7 times that shown for CO(1-0).

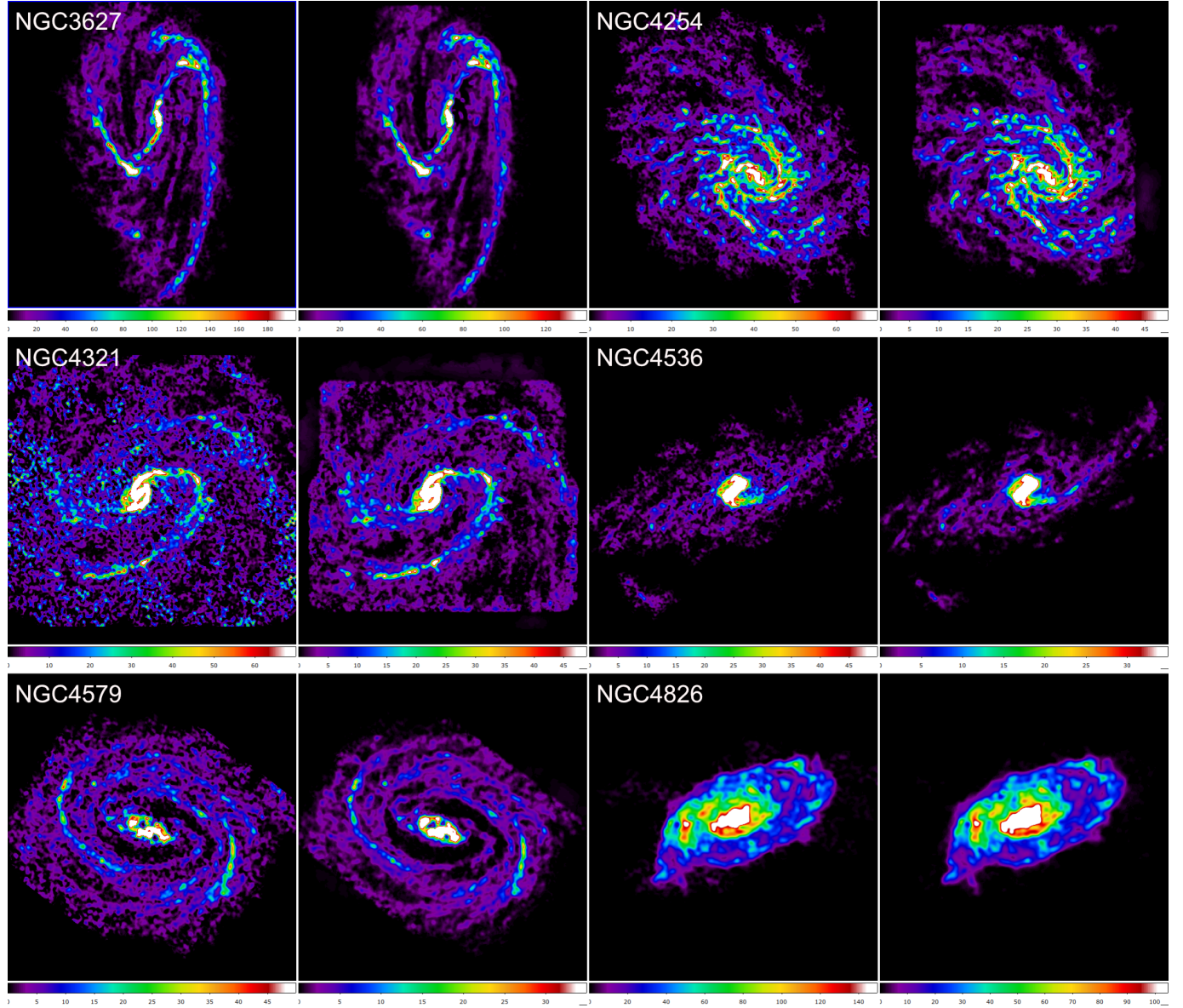
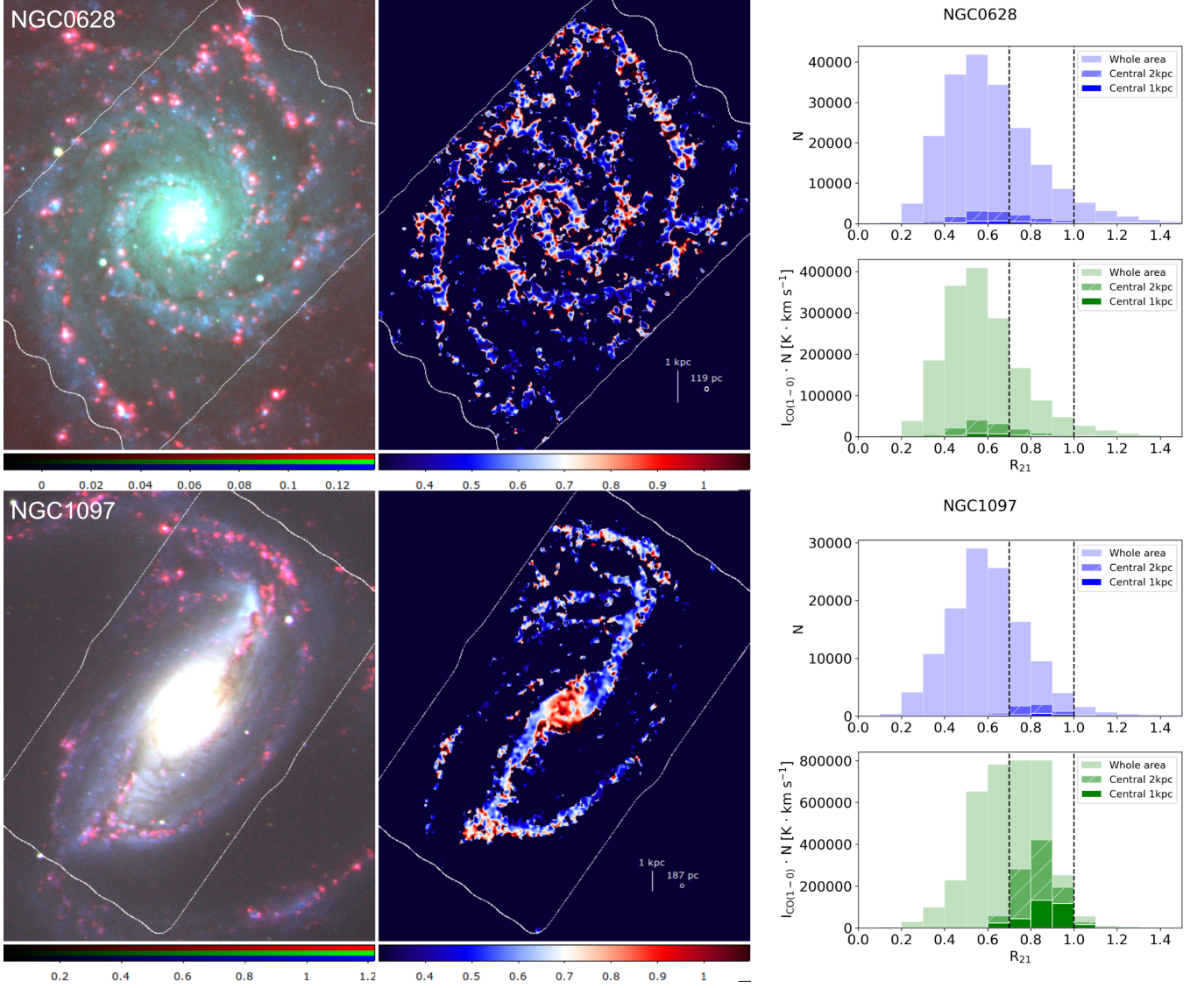


Figure 4. Same as Figure 3 but for NGC3627, NGC4254, NGC4321, NGC4536, NGC4579, NGC4826.



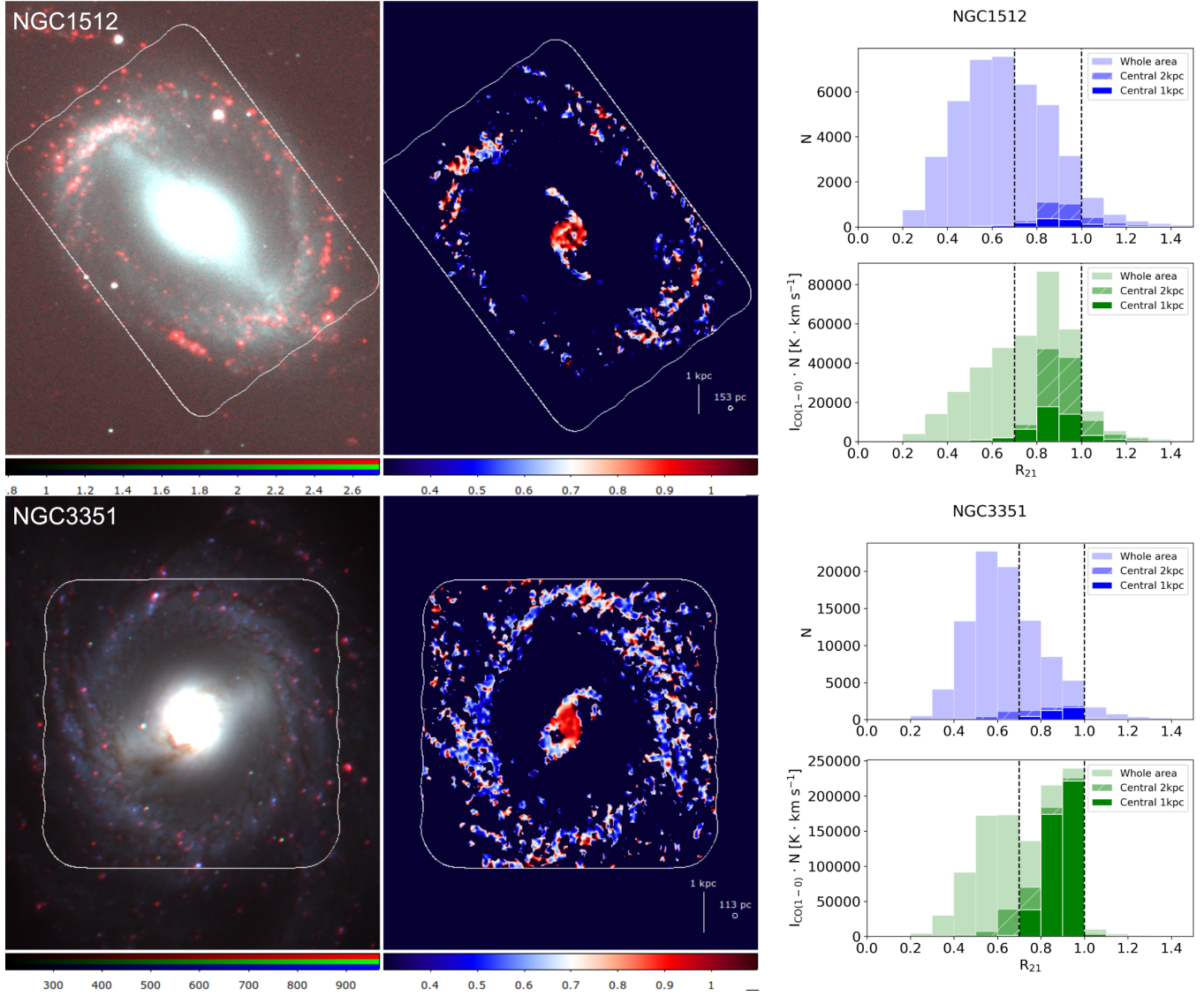


Figure 6. Same as Figure 5 for NGC1512 and NGC3351.

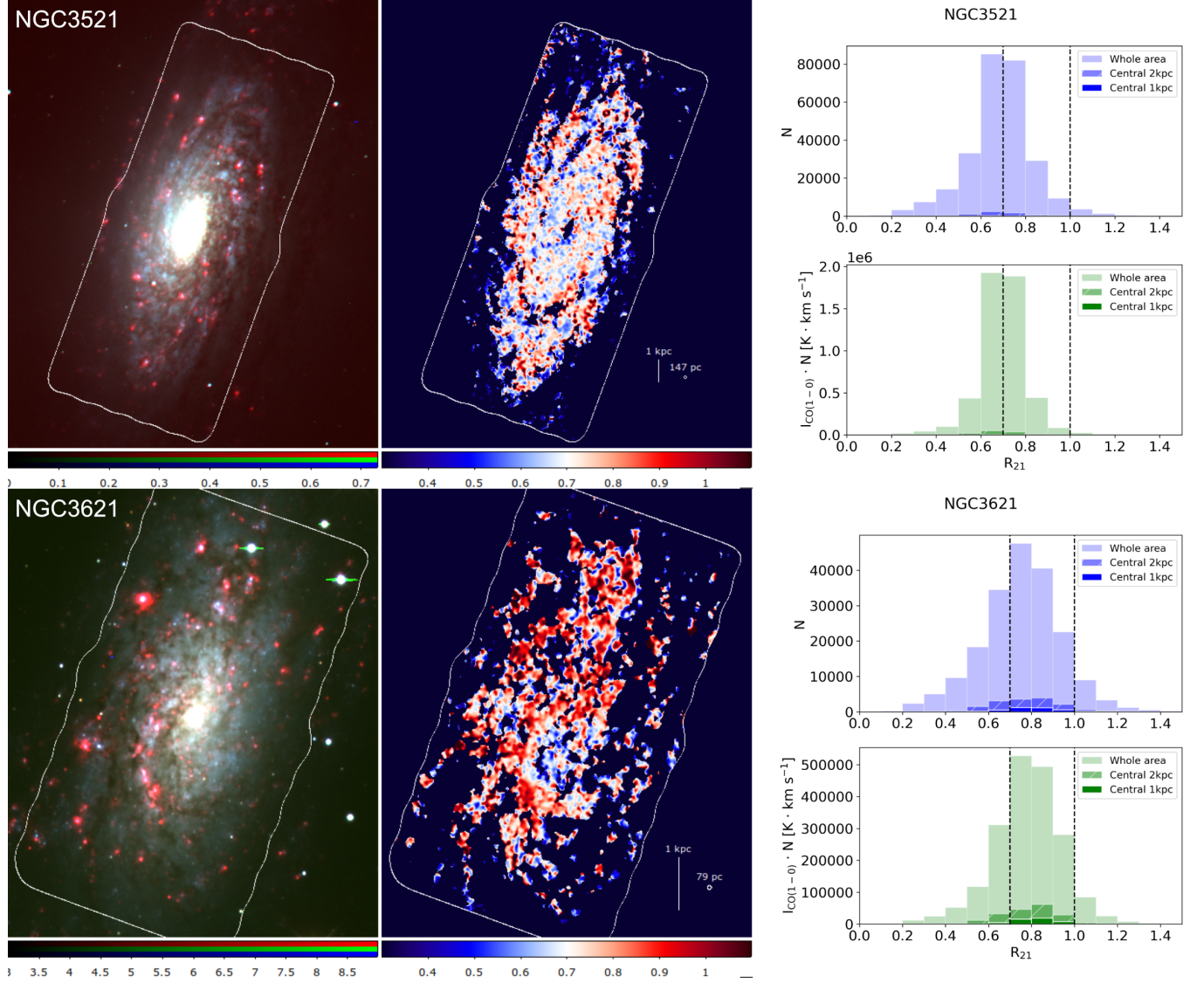


Figure 7. Same as Figure 5 for NGC3521 and NGC3621.

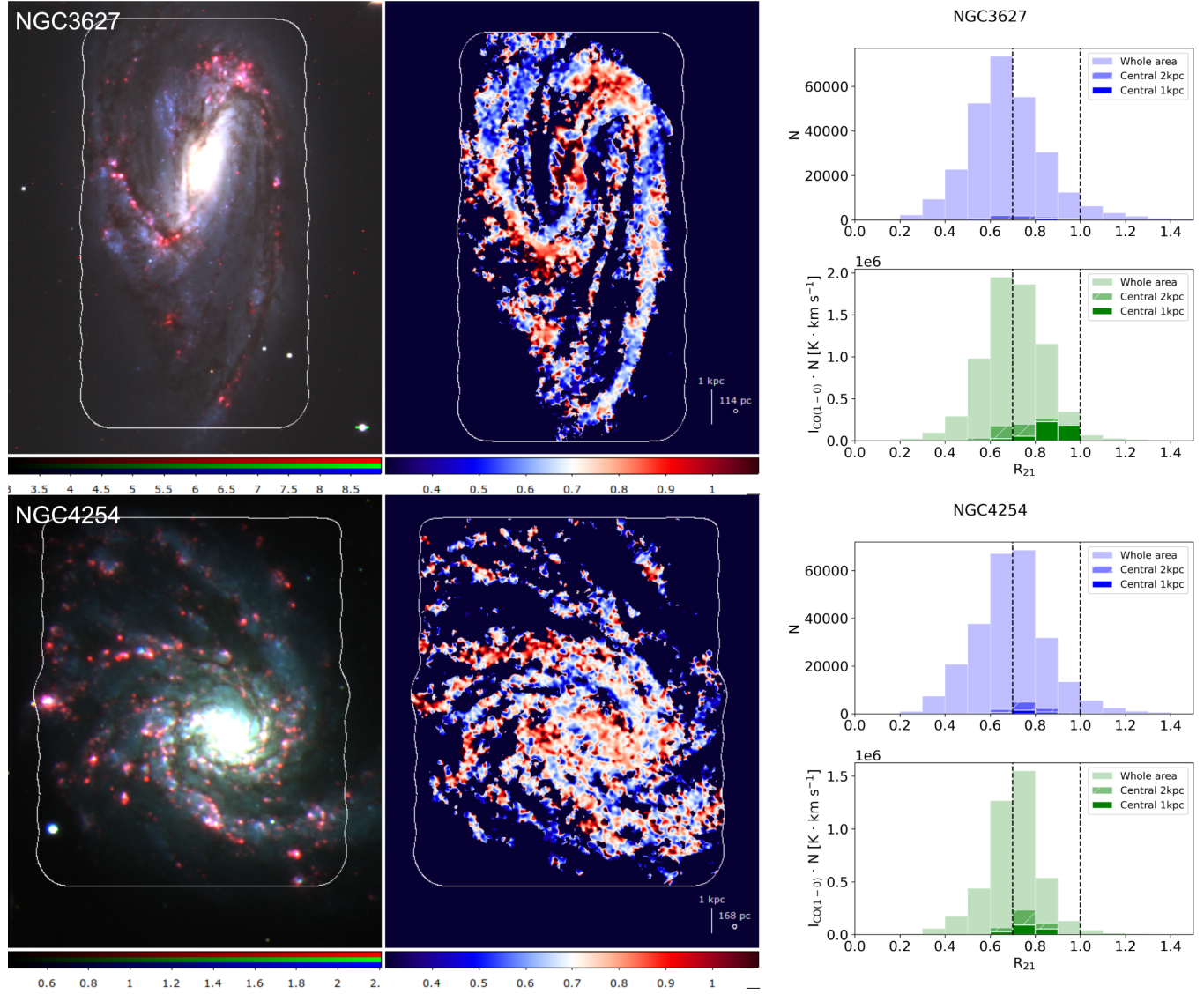


Figure 8. Same as Figure 5 for NGC3627 and NGC4254.

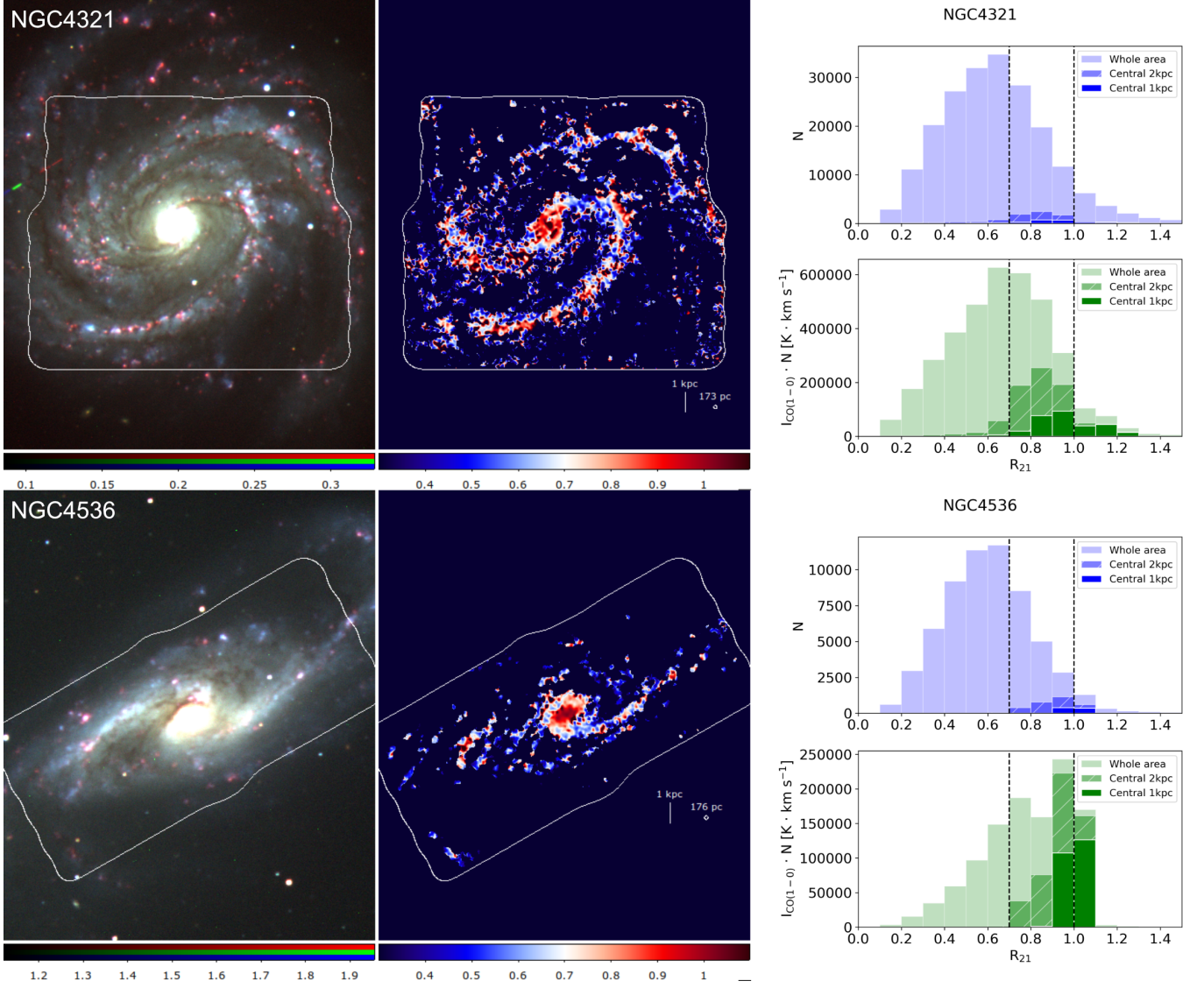


Figure 9. Same as Figure 5 for NGC4321 and NGC4536.

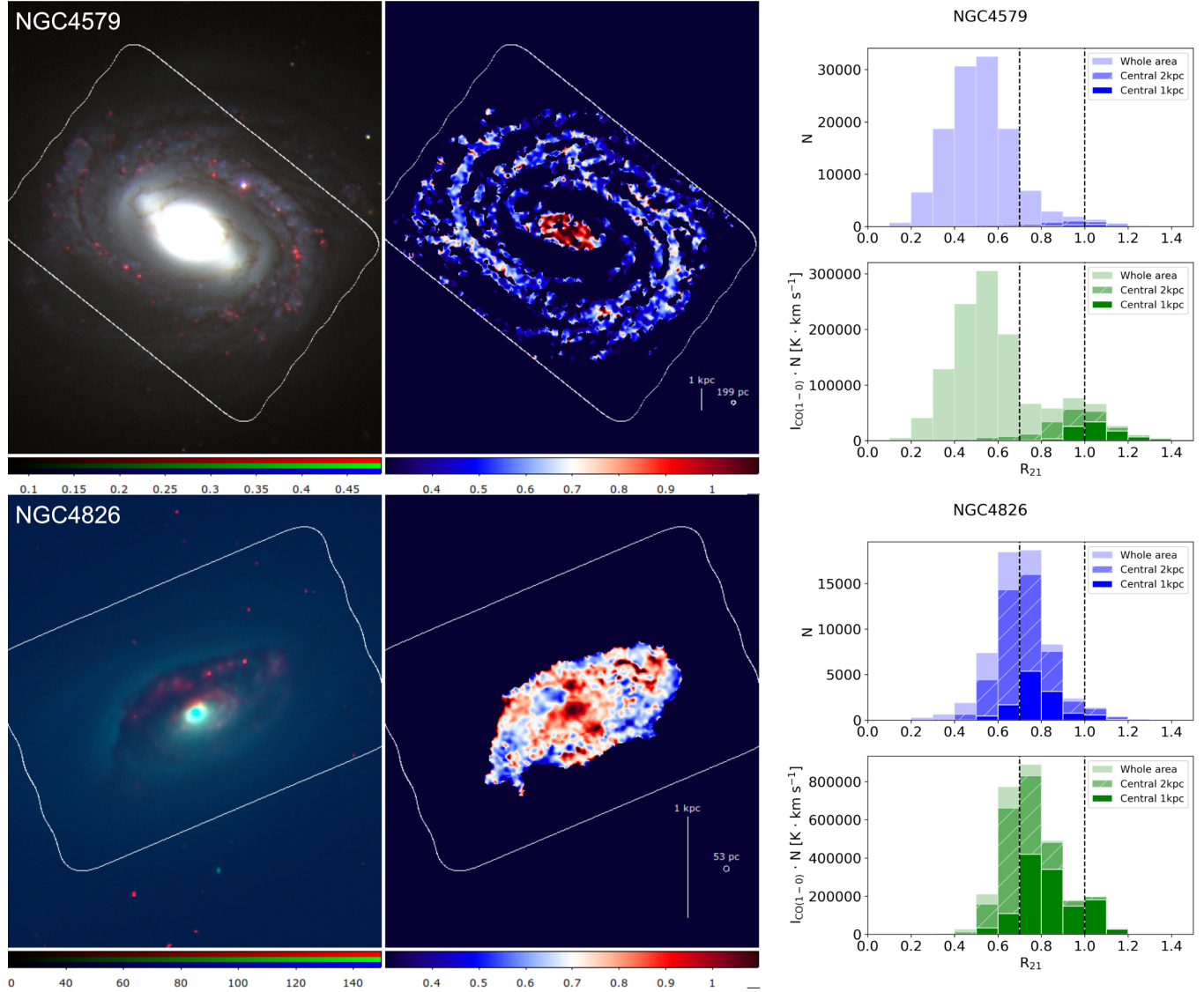


Figure 10. Same as Figure 5 for NGC4579 and NGC4826.

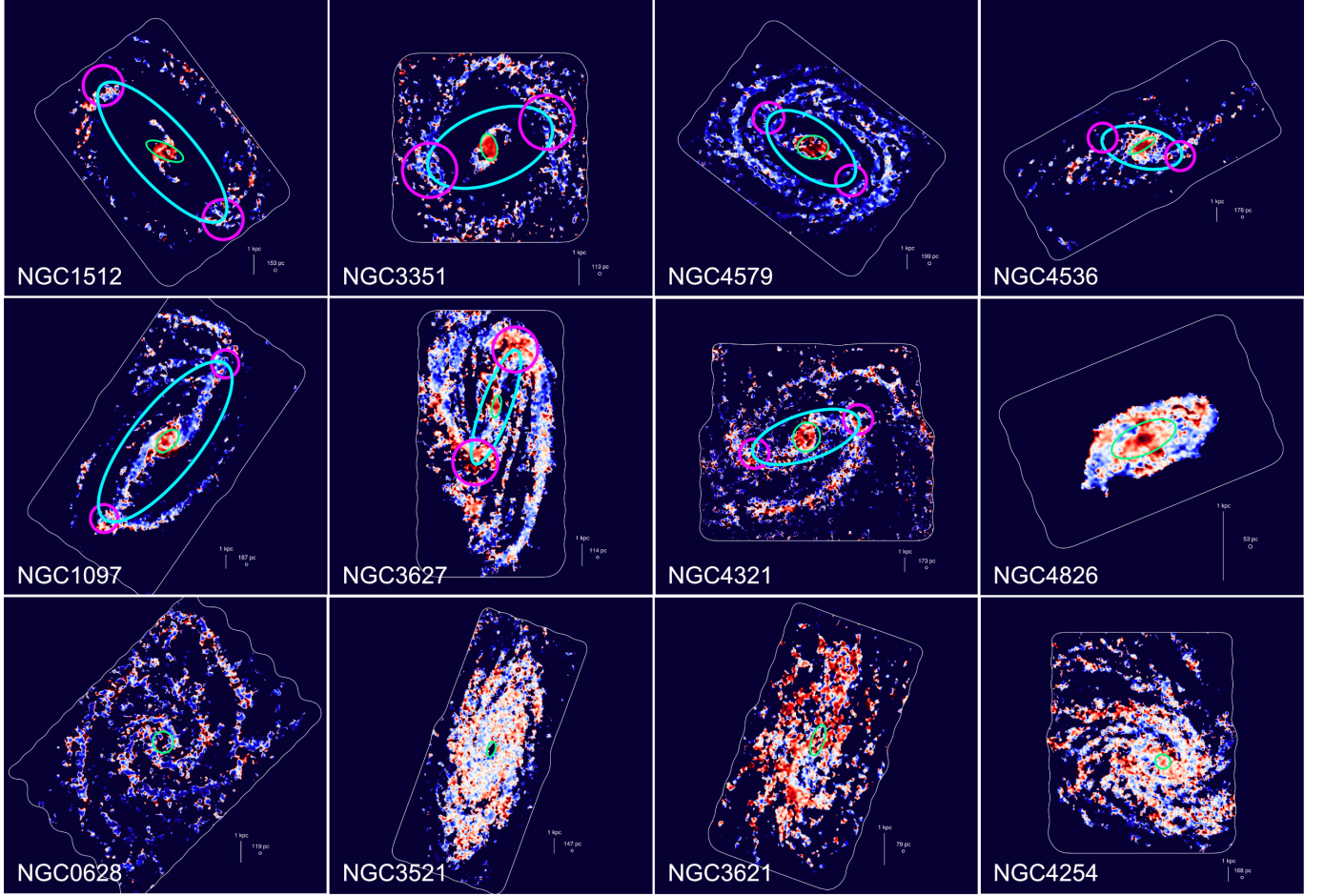


Figure 11. The R_{21} maps arranged according to (1) optical morphology (SB, SAB, SA) and (2) gas morphology for the barred galaxies, following the evolutionary sequence presented in section 5.1.1. The adopted region definitions for the galactic structures are overlaid (section 5.2.5). The central regions (1 or 2 kpc) and the bar ends (2 kpc circles) are enclosed in green and magenta, respectively. The bar regions are enclosed in the cyan ellipses, but do not include the bar ends.

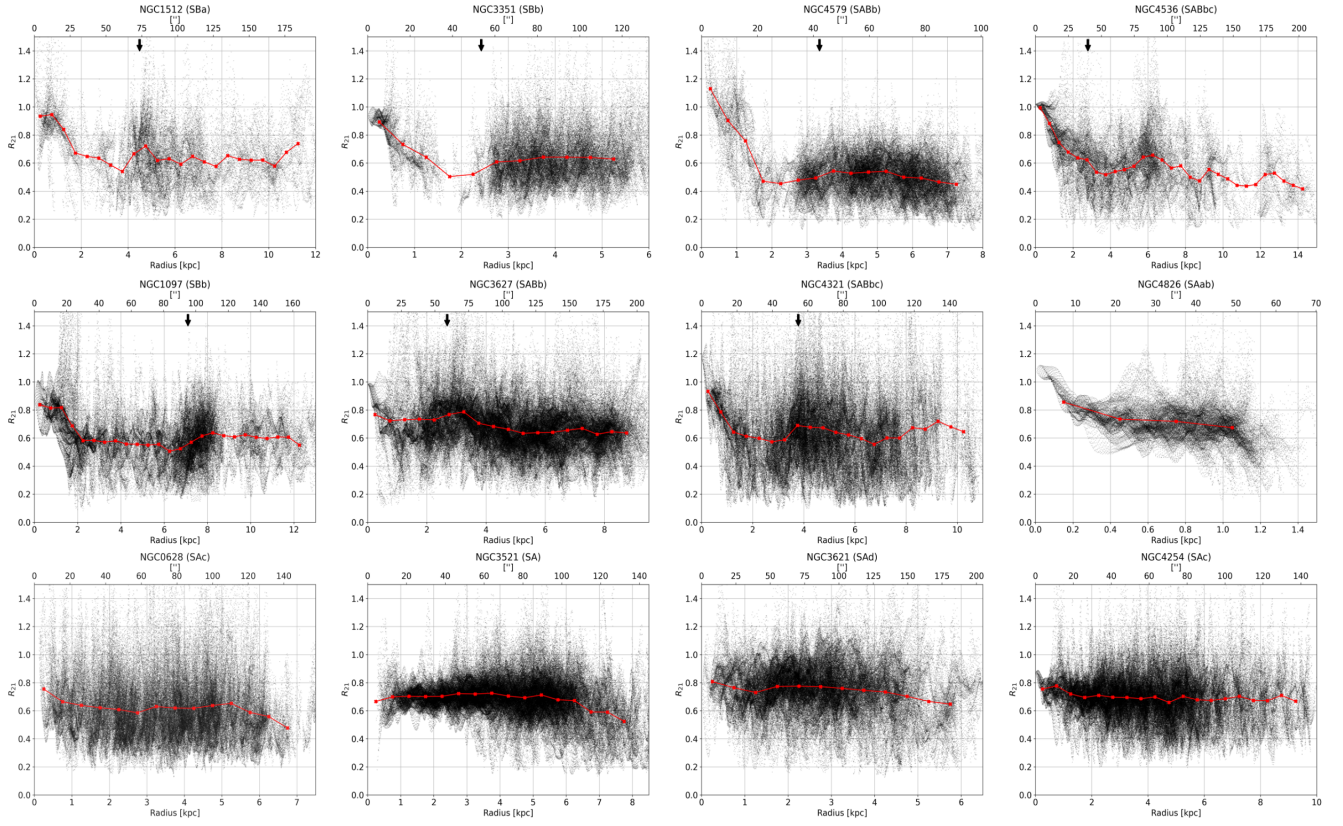


Figure 12. Radial distributions of R_{21} (each pixel) arranged in the same order as Figure 11. The binned means are shown in red. The secondary-axis is in arcseconds and the black arrows indicate the adopted bar lengths (R_{bar}).

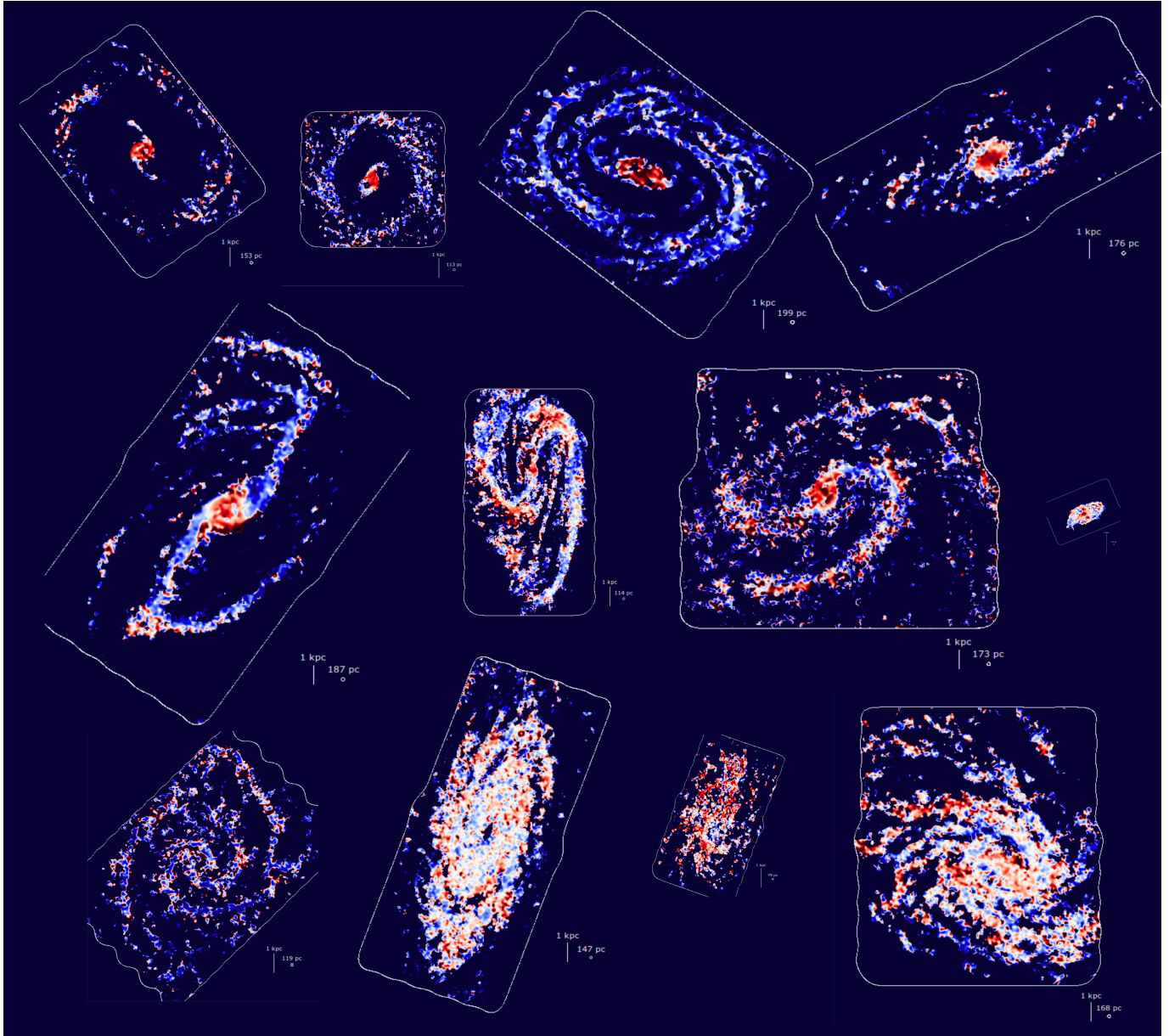


Figure 13. Same as Figure 11 but showing the relative physical sizes of the galaxies.

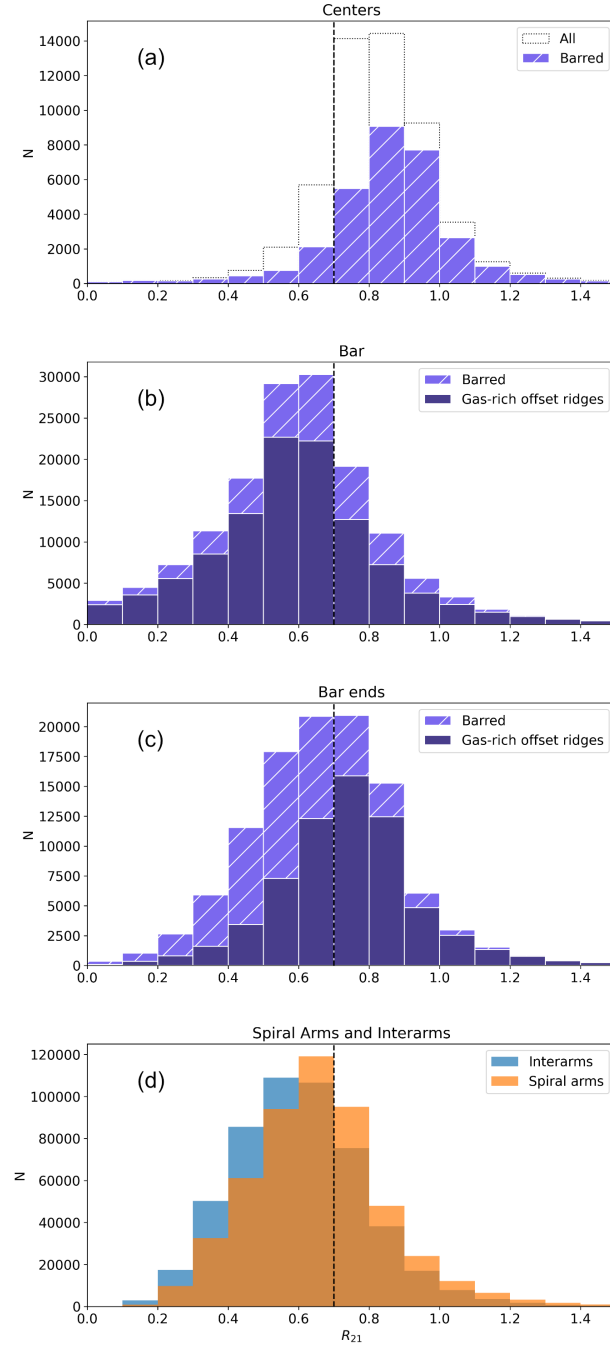


Figure 14. (a-d) R_{21} distributions by number for the center, bar, bar ends, and spiral arms and interarm regions, respectively, using the definitions described in section 5.2.5 and Figure 11. The black dashed line is at $R_{21}=0.7$ for reference. For (a-c) the histograms are shown for all galaxies (dotted), barred galaxies (purple, hatched), and those with the gas-rich offset ridges (dark purple) following the classification introduced in section 5.1.2. For (d) spiral arms are in orange and interarms are in blue.

REFERENCES

- Anand, G. S., Lee, J. C., Van Dyk, S. D., et al. 2021, *MNRAS*, 501, 3621, doi: [10.1093/mnras/staa3668](https://doi.org/10.1093/mnras/staa3668)
- Athanassoula, E. 1992a, *MNRAS*, 259, 328, doi: [10.1093/mnras/259.2.328](https://doi.org/10.1093/mnras/259.2.328)
- . 1992b, *MNRAS*, 259, 345, doi: [10.1093/mnras/259.2.345](https://doi.org/10.1093/mnras/259.2.345)
- Barnes, A. T., Watkins, E. J., Meidt, S. E., et al. 2023, *ApJL*, 944, L22, doi: [10.3847/2041-8213/aca7b9](https://doi.org/10.3847/2041-8213/aca7b9)
- Bolatto, A. D., Wolfire, M., & Leroy, A. K. 2013, *ARA&A*, 51, 207, doi: [10.1146/annurev-astro-082812-140944](https://doi.org/10.1146/annurev-astro-082812-140944)
- CASA Team, Bean, B., Bhatnagar, S., et al. 2022, *PASP*, 134, 114501, doi: [10.1088/1538-3873/ac9642](https://doi.org/10.1088/1538-3873/ac9642)
- Crosthwaite, L. P., & Turner, J. L. 2007, *AJ*, 134, 1827, doi: [10.1086/521645](https://doi.org/10.1086/521645)
- Crosthwaite, L. P., Turner, J. L., Buchholz, L., Ho, P. T. P., & Martin, R. N. 2002, *AJ*, 123, 1892, doi: [10.1086/339479](https://doi.org/10.1086/339479)
- de Vaucouleurs, G., de Vaucouleurs, A., Corwin, Herold G., J., et al. 1991, *Third Reference Catalogue of Bright Galaxies*
- den Brok, J. S., Chatzigiannakis, D., Bigiel, F., et al. 2021, *MNRAS*, 504, 3221, doi: [10.1093/mnras/stab859](https://doi.org/10.1093/mnras/stab859)
- den Brok, J. S., Leroy, A. K., Usero, A., et al. 2023, *MNRAS*, 526, 6347, doi: [10.1093/mnras/stad3091](https://doi.org/10.1093/mnras/stad3091)
- Díaz-García, S., Salo, H., Laurikainen, E., & Herrera-Endoqui, M. 2016, *A&A*, 587, A160, doi: [10.1051/0004-6361/201526161](https://doi.org/10.1051/0004-6361/201526161)
- Downes, D., Reynaud, D., Solomon, P. M., & Radford, S. J. E. 1996, *ApJ*, 461, 186, doi: [10.1086/177046](https://doi.org/10.1086/177046)
- Egusa, F., Gao, Y., Morokuma-Matsui, K., Liu, G., & Maeda, F. 2022, *ApJ*, 935, 64, doi: [10.3847/1538-4357/ac8050](https://doi.org/10.3847/1538-4357/ac8050)
- Falgarone, E., Panis, J. F., Heithausen, A., et al. 1998, *A&A*, 331, 669
- Freedman, W. L., Madore, B. F., Gibson, B. K., et al. 2001, *ApJ*, 553, 47, doi: [10.1086/320638](https://doi.org/10.1086/320638)
- García-Burillo, S., Guelin, M., & Cernicharo, J. 1993, *A&A*, 274, 123
- Goldreich, P., & Kwan, J. 1974, *ApJ*, 189, 441, doi: [10.1086/152821](https://doi.org/10.1086/152821)
- Hasegawa, T. 1997, in *IAU Symposium*, Vol. 170, IAU Symposium, ed. W. B. Latter, S. J. E. Radford, P. R. Jewell, J. G. Mangum, & J. Bally, 39–46
- Herrera-Endoqui, M., Díaz-García, S., Laurikainen, E., & Salo, H. 2015, *A&A*, 582, A86, doi: [10.1051/0004-6361/201526047](https://doi.org/10.1051/0004-6361/201526047)
- Hidaka, M., & Sofue, Y. 2002, *PASJ*, 54, 33, doi: [10.1093/pasj/54.1.33](https://doi.org/10.1093/pasj/54.1.33)
- Ho, L. C., Filippenko, A. V., & Sargent, W. L. W. 1997, *ApJ*, 487, 591, doi: [10.1086/304643](https://doi.org/10.1086/304643)
- Kennicutt, R. C., Calzetti, D., Aniano, G., et al. 2011, *PASP*, 123, 1347, doi: [10.1086/663818](https://doi.org/10.1086/663818)
- Kennicutt, Jr., R. C., Armus, L., Bendo, G., et al. 2003, *PASP*, 115, 928, doi: [10.1086/376941](https://doi.org/10.1086/376941)
- Koda, J., Egusa, F., Hirota, A., et al. 2025, *ApJ*, 986, 29, doi: [10.3847/1538-4357/add1dc](https://doi.org/10.3847/1538-4357/add1dc)
- Koda, J., & Sofue, Y. 2006, *PASJ*, 58, 299, doi: [10.1093/pasj/58.2.299](https://doi.org/10.1093/pasj/58.2.299)
- Koda, J., Scoville, N., Hasegawa, T., et al. 2012, *ApJ*, 761, 41, doi: [10.1088/0004-637X/761/1/41](https://doi.org/10.1088/0004-637X/761/1/41)
- Koda, J., Sawada, T., Sakamoto, K., et al. 2020, *ApJL*, 890, L10, doi: [10.3847/2041-8213/ab70b7](https://doi.org/10.3847/2041-8213/ab70b7)
- Koda, J., Hirota, A., Egusa, F., et al. 2023, *ApJ*, 949, 108, doi: [10.3847/1538-4357/acc65e](https://doi.org/10.3847/1538-4357/acc65e)
- Komugi, S., Sawada, T., Koda, J., et al. 2025, *ApJ*, 980, 126, doi: [10.3847/1538-4357/ada6b5](https://doi.org/10.3847/1538-4357/ada6b5)
- Kuno, N., Sato, N., Nakanishi, H., et al. 2007, *PASJ*, 59, 117, doi: [10.1093/pasj/59.1.117](https://doi.org/10.1093/pasj/59.1.117)
- Leroy, A. K., Schinnerer, E., Hughes, A., et al. 2021, *ApJS*, 257, 43, doi: [10.3847/1538-4365/ac17f3](https://doi.org/10.3847/1538-4365/ac17f3)
- Leroy, A. K., Rosolowsky, E., Usero, A., et al. 2022, *ApJ*, 927, 149, doi: [10.3847/1538-4357/ac3490](https://doi.org/10.3847/1538-4357/ac3490)
- Lundgren, A. A., Wiklind, T., Olofsson, H., & Rydbeck, G. 2004, *A&A*, 413, 505, doi: [10.1051/0004-6361:20031507](https://doi.org/10.1051/0004-6361:20031507)
- Maeda, F., Egusa, F., Ohta, K., Fujimoto, Y., & Habe, A. 2023, *ApJ*, 943, 7, doi: [10.3847/1538-4357/aca664](https://doi.org/10.3847/1538-4357/aca664)
- Maeda, F., Egusa, F., Ohta, K., et al. 2022, *ApJ*, 926, 96, doi: [10.3847/1538-4357/ac4505](https://doi.org/10.3847/1538-4357/ac4505)
- Maeda, F., Ohta, K., Egusa, F., et al. 2025, *ApJ*, 981, 156, doi: [10.3847/1538-4357/adb41e](https://doi.org/10.3847/1538-4357/adb41e)
- Makarov, D., Prugniel, P., Terekhova, N., Courtois, H., & Vauglin, I. 2014, *A&A*, 570, A13, doi: [10.1051/0004-6361/201423496](https://doi.org/10.1051/0004-6361/201423496)
- Mazzalay, X., Maciejewski, W., Erwin, P., et al. 2014, *MNRAS*, 438, 2036, doi: [10.1093/mnras/stt2319](https://doi.org/10.1093/mnras/stt2319)
- McQuinn, K. B. W., Skillman, E. D., Dolphin, A. E., Berg, D., & Kennicutt, R. 2017, *AJ*, 154, 51, doi: [10.3847/1538-3881/aa7aad](https://doi.org/10.3847/1538-3881/aa7aad)
- Momose, R., Okumura, S. K., Koda, J., & Sawada, T. 2010, *ApJ*, 721, 383, doi: [10.1088/0004-637X/721/1/383](https://doi.org/10.1088/0004-637X/721/1/383)
- Nishimura, A., Tokuda, K., Kimura, K., et al. 2015, *ApJS*, 216, 18, doi: [10.1088/0067-0049/216/1/18](https://doi.org/10.1088/0067-0049/216/1/18)
- Oka, T., Hasegawa, T., Handa, T., Hayashi, M., & Sakamoto, S. 1996, *ApJ*, 460, 334, doi: [10.1086/176973](https://doi.org/10.1086/176973)
- Oka, T., Hasegawa, T., Hayashi, M., Handa, T., & Sakamoto, S. 1998a, *ApJ*, 493, 730, doi: [10.1086/305133](https://doi.org/10.1086/305133)
- Oka, T., Hasegawa, T., Sato, F., Tsuboi, M., & Miyazaki, A. 1998b, *ApJS*, 118, 455, doi: [10.1086/313138](https://doi.org/10.1086/313138)

- Querejeta, M., Schinnerer, E., Meidt, S., et al. 2021, *A&A*, 656, A133, doi: [10.1051/0004-6361/202140695](https://doi.org/10.1051/0004-6361/202140695)
- Rodríguez, M. J., Lee, J. C., Indebetouw, R., et al. 2024, Tracing the earliest stages of star and cluster formation in 19 nearby galaxies with PHANGS-JWST and HST: compact 3.3 μ m PAH emitters and their relation to the optical census of star clusters.
<https://arxiv.org/abs/2412.07862>
- S4G Team. 2020, Spitzer Survey of Stellar Structure in Galaxies, IPAC, doi: [10.26131/IRSA425](https://doi.org/10.26131/IRSA425)
- Sakamoto, K., Okumura, S. K., Ishizuki, S., & Scoville, N. Z. 1999, *ApJ*, 525, 691, doi: [10.1086/307910](https://doi.org/10.1086/307910)
- Sakamoto, S., Hasegawa, T., Handa, T., Hayashi, M., & Oka, T. 1997, *ApJ*, 486, 276, doi: [10.1086/304479](https://doi.org/10.1086/304479)
- Sakamoto, S., Hayashi, M., Hasegawa, T., Handa, T., & Oka, T. 1994, *ApJ*, 425, 641, doi: [10.1086/174011](https://doi.org/10.1086/174011)
- Sault, R. J., Staveley-Smith, L., & Brouw, W. N. 1996, *A&AS*, 120, 375
- Sault, R. J., Teuben, P. J., & Wright, M. C. H. 1995, in *Astronomical Society of the Pacific Conference Series*, Vol. 77, *Astronomical Data Analysis Software and Systems IV*, ed. R. A. Shaw, H. E. Payne, & J. J. E. Hayes, 433, doi: [10.48550/arXiv.astro-ph/0612759](https://doi.org/10.48550/arXiv.astro-ph/0612759)
- Sawada, T., Hasegawa, T., Handa, T., et al. 2001, *ApJS*, 136, 189, doi: [10.1086/321793](https://doi.org/10.1086/321793)
- Scoville, N. Z., & Solomon, P. M. 1974, *ApJL*, 187, L67, doi: [10.1086/181398](https://doi.org/10.1086/181398)
- Sellwood, J. A., & Wilkinson, A. 1993, *Reports on Progress in Physics*, 56, 173, doi: [10.1088/0034-4885/56/2/001](https://doi.org/10.1088/0034-4885/56/2/001)
- Seta, M., Hasegawa, T., Dame, T. M., et al. 1998, *ApJ*, 505, 286, doi: [10.1086/306141](https://doi.org/10.1086/306141)
- Sheth, K., Vogel, S. N., Regan, M. W., et al. 2002, *AJ*, 124, 2581, doi: [10.1086/343835](https://doi.org/10.1086/343835)
- Sheth, K., Vogel, S. N., Regan, M. W., Thornley, M. D., & Teuben, P. J. 2005, *ApJ*, 632, 217, doi: [10.1086/432409](https://doi.org/10.1086/432409)
- Sheth, K., Regan, M., Hinz, J. L., et al. 2010, *PASP*, 122, 1397, doi: [10.1086/657638](https://doi.org/10.1086/657638)
- SINGS Team. 2020, Spitzer Infrared Nearby Galaxy Survey, IPAC, doi: [10.26131/IRSA424](https://doi.org/10.26131/IRSA424)
- Sorai, K., Kuno, N., Muraoka, K., et al. 2019, *PASJ*, 71, S14, doi: [10.1093/pasj/psz115](https://doi.org/10.1093/pasj/psz115)
- Tully, R. B., Courtois, H. M., & Sorce, J. G. 2016, *AJ*, 152, 50, doi: [10.3847/0004-6256/152/2/50](https://doi.org/10.3847/0004-6256/152/2/50)
- Tully, R. B., Courtois, H. M., Dolphin, A. E., et al. 2013, *AJ*, 146, 86, doi: [10.1088/0004-6256/146/4/86](https://doi.org/10.1088/0004-6256/146/4/86)
- van der Tak, F. F. S., Black, J. H., Schöier, F. L., Jansen, D. J., & van Dishoeck, E. F. 2007, *A&A*, 468, 627, doi: [10.1051/0004-6361:20066820](https://doi.org/10.1051/0004-6361:20066820)
- Véron-Cetty, M. P., & Véron, P. 2010, *A&A*, 518, A10, doi: [10.1051/0004-6361/201014188](https://doi.org/10.1051/0004-6361/201014188)
- Wada, K. 1994, *PASJ*, 46, 165
- Yajima, Y., Sorai, K., Miyamoto, Y., et al. 2021, *PASJ*, 73, 257, doi: [10.1093/pasj/psaa119](https://doi.org/10.1093/pasj/psaa119)
- Yu, S.-Y., Kalinova, V., Colombo, D., et al. 2022, *A&A*, 666, A175, doi: [10.1051/0004-6361/202244306](https://doi.org/10.1051/0004-6361/202244306)

This work makes use of the following ALMA data: ADS/JAO.ALMA#2012.1.00650.S, 2015.1.00925.S, 2015.1.00956.S, 2017.1.00886.L, and 2018.1.01651.S, 2022.1.00360.S. ALMA is a partnership of ESO (representing its member states), NSF (USA) and NINS (Japan), together with NRC (Canada), MOST and ASIAA (Taiwan), and KASI (Republic of Korea), in cooperation with the Republic of Chile. The Joint ALMA Observatory is operated by ESO, AUI/NRAO and NAOJ. The National Radio Astronomy Observatory is a facility of the National Science Foundation operated under cooperative agreement by Associated Universities, Inc..

This research has made use of the NASA/IPAC Infrared Science Archive, which is funded by the National Aeronautics and Space Administration and operated by the California Institute of Technology. This research has made use of the NASA/IPAC Extragalactic Database (NED), which is operated by the Jet Propulsion Laboratory, California Institute of Technology, under contract with the National Aeronautics and Space Administration.

JK acknowledges support from NSF through grants AST-2006600 and AST-2406608. F.M. is supported by JSPS KAKENHI grant No. JP23K13142.